Geophysical Journal International

*Geophys. J. Int.* (2014) **199,** 1713–1738 doi: 10.1093/gji/ggu356
GJI Seismology

# An anisotropic shear velocity model of the Earth's mantle using normal modes, body waves, surface waves and long-period waveforms

P. Moulik and G. Ekström

*Lamont-Doherty Earth Observatory of Columbia University, Palisades, NY* 10964*, USA. E-mail: moulik@ldeo.columbia.edu*

Accepted 2014 September 8. Received 2014 August 21; in original form 2014 May 1

## SUMMARY

We use normal-mode splitting functions in addition to surface wave phase anomalies, body wave traveltimes and long-period waveforms to construct a 3-D model of anisotropic shear wave velocity in the Earth's mantle. Our modelling approach inverts for mantle velocity and anisotropy as well as transition-zone discontinuity topographies, and incorporates new crustal corrections for the splitting functions that are consistent with the non-linear corrections we employ for the waveforms. Our preferred anisotropic model, S362ANI+M, is an update to the earlier model S362ANI, which did not include normal-mode splitting functions in its derivation. The new model has stronger isotropic velocity anomalies in the transition zone and slightly smaller anomalies in the lowermost mantle, as compared with S362ANI. The differences in the mid- to lowermost mantle are primarily restricted to features in the Southern Hemisphere. We compare the isotropic part of S362ANI+M with other recent global tomographic models and show that the level of agreement is higher now than in the earlier generation of models, especially in the transition zone and the lower mantle. The anisotropic part of S362ANI+M is restricted to the upper 300 km in the mantle and is similar to S362ANI. When radial anisotropy is allowed throughout the mantle, large-scale anisotropic patterns are observed in the lowermost mantle with $v_{SV} > v_{SH}$ beneath Africa and South Pacific and $v_{SH} > v_{SV}$ beneath several circum-Pacific regions. The transition zone exhibits localized anisotropic anomalies of ∼3 per cent $v_{SH} > v_{SV}$ beneath North America and the Northwest Pacific and ∼2 per cent $v_{SV} > v_{SH}$ beneath South America. However, small improvements in fits to the data on adding anisotropy at depth leave the question open on whether large-scale radial anisotropy is required in the transition zone and in the lower mantle. We demonstrate the potential of mode-splitting data in reducing the trade-offs between isotropic velocity and anisotropy in the lowermost mantle for the even-degree variations. Spurious anisotropic variations in the mid-mantle are also suppressed with the addition of mode-splitting data.

**Key words:** Mantle processes; Body waves; Surface waves and free oscillations; Seismic anisotropy; Seismic tomography; Computational seismology.



## 1 INTRODUCTION

Rapid progress in imaging the Earth has been driven by the improved coverage of seismic stations and our ability to analyse the data collected using theoretical and computational advancements. Several recent studies have attempted to resolve the elastic structure of the mantle with increasing detail and complexity (e.g. Houser *et al.* 2008b; Kustowski *et al.* 2008; Panning *et al.* 2010; Ritsema *et al.* 2010; Simmons *et al.* 2010; Lekić & Romanowicz 2011; Debayle & Ricard 2012; French *et al.* 2013; Chang *et al.* 2014). There is growing agreement between tomographic models of isotropic shear velocity on several large-scale features in the Earth's mantle; most models show similar signatures of continental roots, cooling oceanic plates, subducting slabs and large slow-velocity 'superplumes' at the base of the mantle. Similarity of large-scale variations is important for demonstrating the robustness of tomographic imaging, and offers the prospect of future agreement on smaller length scales, for which the intermodel correlations remain low (Becker & Boschi 2002). Discrepancies between models can either be due to limited data coverage, use of different data sets, or modelling approaches like crustal correction, regularization and parametrization schemes (e.g. Boschi & Dziewoński 1999; Kustowski *et al.* 2007; Meier *et al.* 2007; Ferreira *et al.* 2010; Panning *et al.* 2010; Burgos *et al.* 2014). Large-scale features in the

mantle should be more easily recovered, especially since the spectrum of mantle heterogeneity and therefore its signal is dominated by the long-wavelength components (Su & Dziewoński 1991, 1992). However, there remain aspects on which tomographic models differ, even in their large-scale variations.

For example, current models disagree on the level of large-scale (∼4000 km) heterogeneity in the transition zone and mid-mantle (e.g. Ritsema *et al.* 2010). The transition zone influences the ultimate fate of descending slabs and could act as a high-water-solubility filter for incompatible elements, which would have implications for mantle geodynamics (e.g. Goes *et al.* 2008) and geochemistry (e.g. Bercovici & Karato 2003). Some tomographic studies, using body wave traveltimes, have suggested the continuity of slabs down to the lowermost mantle (e.g. Grand *et al.* 1997; van der Hilst *et al.* 1997) although this has been a subject of debate (e.g. Boschi & Dziewoński 1999). Other studies have used diverse long-period data sets to show a decrease in the strength of the anomalies in the lower mantle (e.g. Gu *et al.* 2001), large lateral extent of faster-than-average anomalies at the base of the transition zone as well as depressions of the 650-km discontinuity underlying the slab-like anomalies (Shearer & Masters 1992; Flanagan & Shearer 1998; Gu *et al.* 2003; Ritsema *et al.* 2004; Panning & Romanowicz 2006; Kustowski *et al.* 2008). These observations suggest an accumulation of subducted mantle material and horizontal flattening of the slabs as proposed by Fukao *et al.* (1992). Improved imaging of the elastic velocity structure may help resolve the geodynamic significance of the transition zone in modulating the flow of material between the upper and lower mantle.

A second aspect on which models disagree is the existence and strength of large-scale radial anisotropy in the Earth's mantle. Disagreements persist even at the longest wavelengths and only a few anisotropic features in the shallowest ∼200 km are consistent between various models (e.g. Kustowski *et al.* 2008; Chang *et al.* 2014). Radial anisotropy may result from deformation mechanisms in the Earth, either by the crystallographic or lattice preferred orientation (CPO, LPO) of anisotropic minerals or by the shape preferred orientation (SPO) of distinct isotropic materials such as in partial melt (Nicolas & Christensen 1987; Karato 1992; Mainprice *et al.* 2000; Karato *et al.* 2008). The anisotropic variations can be used to address questions on mantle rheology and on planetary-scale dynamics such as the evolution of plate motions (e.g. Gaboret *et al.* 2003; Becker *et al.* 2003, 2008; Long & Becker 2010). Various studies have reported strong or localized anisotropy in the uppermost mantle beneath oceanic (e.g. Ekström & Dziewoński 1998; Panning & Romanowicz 2006) and continental lithosphere (e.g. Gung *et al.* 2003; Marone & Romanowicz 2007; Nettles & Dziewoński 2008) as well as in the transition zone (e.g. Fouch & Fischer 1996; Trampert & van Heijst 2002; Chen & Brudzinski 2003; Beghein & Trampert 2004; Yuan & Beghein 2013), mid-mantle (e.g. Wookey *et al.* 2002; Foley & Long 2011) and the lowermost mantle (e.g. Kendall & Silver 1996; Lay *et al.* 1998; Pulliam & Sen 1998; Long 2009; Nowacki *et al.* 2010). However, the presence of large-scale or ubiquitous anisotropy is debated, especially in the transition zone and the deepest mantle (e.g. Panning & Romanowicz 2004, 2006; Kustowski *et al.* 2008).

Improved resolution of these features is hampered by uneven spatial coverage from broad-band seismic stations (e.g. Romanowicz & Giardini 2001; Romanowicz 2003, 2008), especially in the oceans (e.g. Wysession 1996; Webb 1998; Simons *et al.* 2009). The sampling of seismic data is poorest in the Southern Hemisphere. In case of anisotropy, the resolution is also hampered by trade-offs between isotropic and anisotropic structure. Several studies have demonstrated that the isotropic shear velocity structure can contain artefacts if anisotropy is not taken into consideration (e.g. Anderson & Dziewoński 1982; Ekström 2011). Kustowski *et al.* (2008) reported a severe trade-off between the radially anisotropic and isotropic variations in the lowermost mantle, even with the inclusion of several types of diverse data sets.

It is particularly difficult to constrain heterogeneity in the transition zone and mid-mantle due to the limited localized sampling provided by most types of seismic data. Fundamental-mode surface waves provide excellent global coverage (e.g. Trampert & Woodhouse 1995; Laske & Masters 1996; Zhang & Lay 1996; Ekström *et al.* 1997; Ekström 2011) but only constrain the uppermost mantle while teleseismic body waves have uneven sampling in the transition zone (e.g. Fukao *et al.* 1992; van der Hilst *et al.* 1997; Boschi & Dziewoński 1999). Overtones can provide important constraints at such depths and can be included in a variety of ways. For example, overtones can be incorporated using long-period body wave waveforms (e.g. Woodhouse & Dziewoński 1984; Kustowski *et al.* 2008; Panning *et al.* 2010), since they can be thought of as the superposition of normal-mode overtones. The spectral peaks of the normal-mode overtones can also be processed to estimate their splitting coefficients (e.g. Ritzwoller *et al.* 1986; Woodhouse *et al.* 1986; Giardini *et al.* 1988; Ritzwoller *et al.* 1988; He & Tromp 1996; Resovsky & Ritzwoller 1998; Masters *et al.* 2000c; Deuss *et al.* 2011, 2013). A third way to include constraints from overtones is to use their dispersion observations. Some methods to specifically isolate and constrain overtone dispersion have been developed (e.g. van Heijst & Woodhouse 1997; Yoshizawa & Kennett 2002a; Visser & Trampert 2008).

An approach to address issues of resolution is to consider jointly the data sets that provide complementary constraints on large-scale Earth structure. Several earlier studies have used diverse types of data for inversions of mantle heterogeneity (e.g. Dziewoński & Woodward 1992; Masters *et al.* 2000a; Gu *et al.* 2001; Ritsema *et al.* 2004). This approach was also used by Kustowski *et al.* (2008) who combined long-period full waveforms (e.g. Woodhouse & Dziewoński 1984), phase velocities of fundamental-mode surface waves (e.g. Ekström *et al.* 1997) and body wave traveltimes (e.g. Liu & Dziewoński 1998) to derive the model S362ANI. One global data set that was not included was normal-mode-splitting observations (e.g. Resovsky & Ritzwoller 1998). Modes, by their very nature, provide global coverage by integrating the volumetric effects of heterogeneity. Normal-mode-splitting data have previously been used to detect anisotropy in the inner core (e.g. Woodhouse *et al.* 1986; Tromp 1993, 1995) and to constrain isotropic velocity in the mantle (e.g. Resovsky & Ritzwoller 1999b; Ritsema *et al.* 1999, 2010; Masters *et al.* 2000a; Beghein *et al.* 2002). Other authors have used only the splitting data to invert for the lateral variations of density (e.g. Ishii & Tromp 1999) or azimuthal anisotropy (Beghein *et al.* 2008) in the mantle.

Here, we extend the work of Kustowski *et al.* (2008) by incorporating a new, large data set of mode-splitting observations. This is the first tomographic study to exploit the sensitivity of mode-splitting data to constrain radial anisotropy in the Earth's mantle jointly with several other types of data. We deliberately limit other data sets to those used by Kustowski *et al.* (2008); this helps us evaluate the potential benefits of including mode-splitting observations in our inversions. The various types of data used in this study and their modelling approaches are described in Section 2. Our joint inversion framework and the new scheme to correct mode-splitting data for the crustal variations are outlined in Section 3. In Section 4,

we describe the fits to the data and features of our models along with the comparison with other studies. We conclude, in Sections 5 and 6, with a discussion of the results.

## 2 DATA AND FORWARD MODELLING

### 2.1 Normal-mode splitting functions

#### *2.1.1 Theoretical background*

In a spherically symmetric, non-rotating earth model, all the $2l + 1$ singlets of a Rayleigh-wave equivalent spheroidal mode ${}_nS_l$ or a Love-wave equivalent toroidal mode ${}_nT_l$ with overtone number $n$ and angular order $l$ vibrate at a degenerate multiplet frequency. The rotation and ellipticity of the Earth cause departure from this degeneracy, resulting in the splitting of the constitutive singlets. Additional splitting can be attributed to the lateral variations in velocity, anisotropy and density as well as the topography of various discontinuities. Splitting coefficients can be used to describe the additional singlet splitting and can be estimated from event–station spectra of multiple earthquakes. The splitting of each mode can be treated in isolation (self-coupling) or in resonance with other modes (cross-coupling). In the self-coupling approximation, the estimated splitting coefficients are sensitive only to the even-degree heterogeneity, while cross-coupling can provide sensitivity also to the odd degrees (e.g. Resovsky & Ritzwoller 1995). The fundamental-mode pairs ${}_0S_l$–${}_0T_{l+1}$, for example, are strongly coupled in the 1.5–3 mHz range, primarily due to the Coriolis force. In this study, we consider observations of self-coupled modes; the small number of available cross-coupled splitting-coefficient observations are not included.

We use perturbation theory to relate the self-coupled splitting coefficients, denoted by $c_{st}$ for an angular order $s$ and azimuthal order $t$ in spherical harmonics, to the corresponding perturbations in the $i$th model parameter $m_i^{st}$, according to

$$c_{st} = \int_0^a \sum_{i=1}^{6} \delta m_i^{st} K_{m_i}^s \, \mathrm{d}r + K_{410}^s \delta h_{410}^{st} + K_{650}^s \delta h_{650}^{st}, \tag{1}$$

where the integral is taken over the radius $r$ from the Earth's centre to the free surface at $a = 6371$ km. We limit our analysis to a transversely isotropic medium without lateral variations in azimuthal anisotropy, which would allow wave speeds to vary with the azimuth of propagation. Therefore, $m_i^{st}$ stands for the five elastic parameters $v_{\mathrm{PH}}$, $v_{\mathrm{PV}}$, $v_{\mathrm{SH}}$, $v_{\mathrm{SV}}$ and $\eta$, as well as the density $\rho$, while $\delta h_{410}^{st}$ and $\delta h_{650}^{st}$ stand for the topography of the 410- and 650-km discontinuities. We use the expressions from Mochizuki (1986) to compute the kernels for $v_{\mathrm{PH}}$, $v_{\mathrm{PV}}$, $v_{\mathrm{SH}}$, $v_{\mathrm{SV}}$ and $\eta$ for the 1-D reference model STW105 (Kustowski *et al.* 2008), while the kernels for $\rho$ and the topography kernels $K_{650}^s$ and $K_{650}^s$ are calculated using the expressions in Woodhouse & Dahlen (1978). Previous 3-D tomographic studies that used mode data (e.g. Ishii & Tromp 1999, 2001; Resovsky & Ritzwoller 1999b; Romanowicz 2001) focused on isotropic velocity heterogeneity; here, we also account for variations in radial anisotropy in the forward and inverse modelling of splitting coefficients.

We visualize the splitting coefficients of a mode using its splitting function $F(\theta, \phi)$ (e.g. Woodhouse *et al.* 1986; Giardini *et al.* 1987), defined as

$$F(\theta, \phi) = \sum_{s=0}^{2l} \sum_{t=-s}^{s} c_{st} Y_s^t(\theta, \phi), \tag{2}$$

where $Y_s^t$ denotes a fully normalized surface spherical harmonic of degree $s$ and order $t$ (Dahlen & Tromp 1998), as described in the Appendix. The 2-D splitting functions are roughly equivalent, at the ray-theoretical limit ($l \gg s$), to the phase velocity maps obtained from surface waves. The values of the splitting function at a given colatitude $\theta$ and longitude $\phi$ can be interpreted as the local variation away from the degenerate frequency of the multiplet, as calculated from the reference 1-D model. The observed splitting functions of the modes ${}_1S_8$, ${}_2S_{12}$, ${}_0T_{10}$ and ${}_1T_9$, with their varying sensitivities at depth to the anisotropic shear velocities $v_{\mathrm{SH}}$, $v_{\mathrm{SV}}$ and its Voigt average $v_S$, are shown in Fig. 1. The spheroidal modes ${}_2S_{12}$ and ${}_1S_8$ are sensitive primarily to the $v_{\mathrm{SV}}$ structure in the upper and lower mantle, showing thereby the even-degree signatures of low-velocity ridges and deep-mantle superplumes, respectively. In contrast, the toroidal modes ${}_0T_{10}$ and ${}_1T_9$ are sensitive to both $v_{\mathrm{SH}}$ and $v_{\mathrm{SV}}$.

Theoretical advancements in conjunction with the availability of data from large earthquakes led to the early measurements of splitting coefficients in the 1990s (Giardini *et al.* 1987, 1988; Ritzwoller *et al.* 1988; Li *et al.* 1991; Tromp & Zanzerkia 1995; He & Tromp 1996; Resovsky & Ritzwoller 1998; Masters *et al.* 2000b). Most of these self-coupled splitting-coefficient observations were made using the iterative spectral-fitting (ISF) technique. Deuss *et al.* (2011) have recently estimated splitting coefficients of spheroidal modes at periods longer than 300 s using the ISF technique. These new splitting data are constrained by a large number of event–station spectra from all $M_{\mathrm{W}} > 7.6$ as well as deep (>100 km) $M_{\mathrm{W}} > 7.4$ earthquakes that occurred during the period 1976–2008. In this recent study, the splitting coefficients are determined for even spherical harmonics up to degree 14.

#### *2.1.2 Selecting the subset of mode-splitting data for inversions*

We compile the results from several studies (Tromp & Zanzerkia 1995; He & Tromp 1996; Resovsky & Ritzwoller 1998; Deuss *et al.* 2011) and perform tests to select the subset of observations to be used in our inversions. We first evaluate the consistency between the splitting-function observations by calculating their correlations ($R$) and average differences ($\Delta F$), given by

$$R = \frac{\int_\Omega F_1^s(\theta, \phi) F_2^s(\theta, \phi) \, \mathrm{d}\Omega}{\left[ \int_\Omega F_1^s(\theta, \phi)^2 \mathrm{d}\Omega \times \int_\Omega F_2^s(\theta, \phi)^2 \mathrm{d}\Omega \right]^{1/2}} \tag{3}$$

and

$$\Delta F = \frac{\int_\Omega |F_1^s(\theta, \phi) - F_2^s(\theta, \phi)| \mathrm{d}\Omega}{|F_1^s(\theta, \phi)|_{\max}}, \tag{4}$$

where $F_1^s$ and $F_2^s$ are the splitting functions from different studies truncated at a given degree $s \leq 2l$, where $l$ is the angular order of the mode. By limiting the expansions of the splitting functions to certain degrees, we can focus on the consistency of features at different wavelengths. We classify the modes common to two studies into three categories based on subjectively chosen values of $\Delta F$ and $R$: 'highly consistent' for those exhibiting small differences ($\Delta F < 0.15$), 'inconsistent' for those that have large differences ($\Delta F \geq 0.15$) and low correlations ($R < 0.6$) and 'consistent' for the remaining modes that differ in their amplitudes ($\Delta F \geq 0.15$) but not in their patterns ($R \geq 0.6$).

We analyse the agreement between pairs of studies by estimating the fraction of highly consistent modes (Table 1). Fewer than half of the modes measured by He & Tromp (1996) and Tromp &

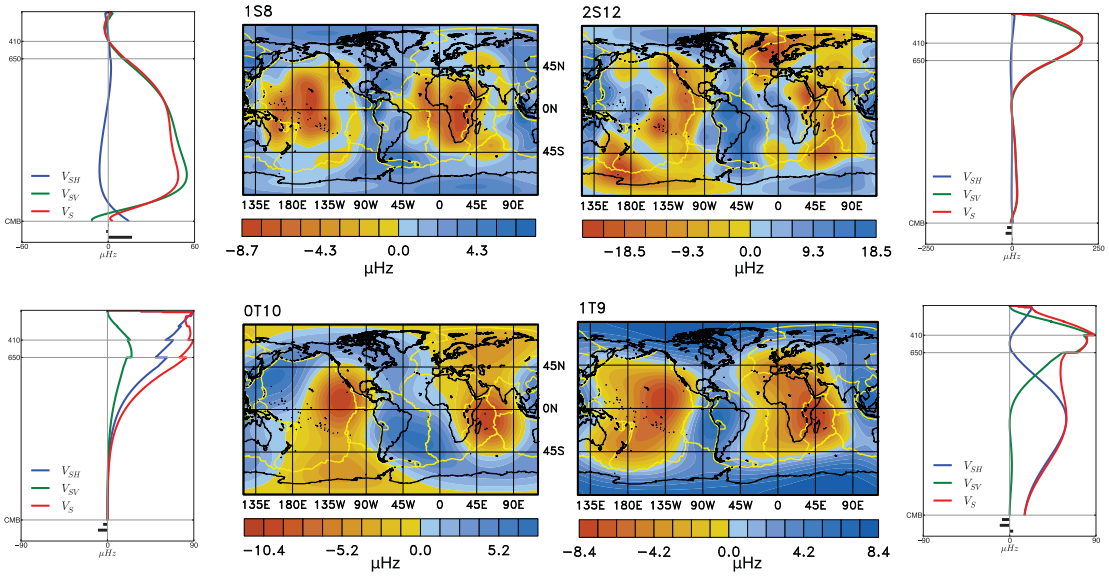


**Figure 1.** The observed splitting functions of four of the modes used in this study. The data for spheroidal modes ${}_1S_8$ and ${}_2S_{12}$ are from Deuss *et al.* (2011), while those for toroidal modes ${}_0T_{10}$ and ${}_1T_9$ are from Resovsky & Ritzwoller (1998). The degree-2 sensitivity kernels, ($K^2_{m_i}$ in eq. 1) calculated using the 1-D reference model STW105 (Kustowski *et al.* 2008), are plotted here for the anisotropic shear velocities $m_i = v_{SH}$, $v_{SV}$ and its Voigt average $v_S$. The depth of the 410- and 650-km discontinuities and the CMB are indicated by grey horizontal lines. The horizontal bars beneath the velocity kernels show from top to bottom, the mode's sensitivity to topographic perturbations of the 410- and 650-km discontinuities and the CMB ($K^2_{410}$, $K^2_{650}$ & $K^2_{CMB}$). Note that the kernels are in units of $\mu$Hz and correspond to variations in $\delta m_i/m_i$ or $\delta h/a$ of 1 per cent, where $a = 6371$ km and that each graph is scaled independently.

**Table 1.** Fraction of highly consistent versus total modes common to pairs of catalogues. The calculation of $\Delta F$ and $R$ for a mode is truncated at the highest degree for which both catalogues have data available. The sources of the splitting functions are abbreviated as follows: Deuss *et al.* (2011) as D11, Resovsky & Ritzwoller (1998) as R&R, He & Tromp (1996) as HT and Tromp & Zanzerkia (1995) as TZ.

| Highly consistent/Total common modes | | | | |
|---|---|---|---|---|
| | D11 | R&R | HT | TZ |
| D11 | – | 34/54 | 13/32 | – |
| R&R | 34/54 | – | 11/35 | 2/11 |

Zanzerkia (1995) are highly consistent with the ones measured in more recent studies (Resovsky & Ritzwoller 1998; Deuss *et al.* 2011). In contrast, the splitting functions for 34 out of 54 modes common to Resovsky & Ritzwoller (1998) and Deuss *et al.* (2011) are highly consistent. Only 2 out of 11 toroidal modes common to Tromp & Zanzerkia (1995) and Resovsky & Ritzwoller (1998) are highly consistent, and splitting functions for modes ${}_0T_4$ and ${}_1T_1$ are negatively correlated between the studies. We therefore exclude the data from He & Tromp (1996) and Tromp & Zanzerkia (1995) from our inversions and focus on the extensive compilations of Resovsky & Ritzwoller (1998) and Deuss *et al.* (2011), hereafter referred to as R&R and D11, respectively.

Since we are focusing on the elastic heterogeneity in the mantle, we exclude from our analysis modes that have substantial sensitivity to the core: ${}_2S_3$, ${}_3S_1$, ${}_3S_2$, ${}_3S_8$, ${}_5S_2$, ${}_5S_3$, ${}_6S_1$, ${}_6S_3$ and ${}_8S_1$ (Woodhouse *et al.* 1986; He & Tromp 1996; Durek & Romanowicz 1999). We also exclude the modes ${}_4S_1$, ${}_4S_2$, ${}_0T_4$ and ${}_1T_1$, as they are negatively correlated between the various studies. We perform inversions for lateral heterogeneity, as described in the subsequent sections, with and without modes ${}_0S_3$ and ${}_1S_2$ that have low correlations ($R < 0.6$) between the studies. The inverted models give better fits to the D11 data and we therefore exclude the R&R data for these modes as they should be superseded by D11, owing to the expanded data set. Similar experiments do not provide a clear choice for the mode ${}_0S_{11}$ and ${}_0S_{12}$, so we include the coefficients from both studies. We also include the splitting coefficients of the 'football mode' ${}_0S_2$ and the mode ${}_2S_1$, which were measured for the first time by Deuss *et al.* (2011). The resultant composite catalogue (Table 2) of splitting coefficients used in our inversions is highly consistent at degree 2 for the modes common to R&R and D11 (Fig. 2a). This consistency decreases for some modes at higher degrees, especially for the modes with significant cross-coupling such as ${}_0S_{11}$ and ${}_4S_3$. However, 30 out of the 44 modes common to the two catalogues are highly consistent even in their shorter-wavelength ($s \geq 4$) variations (Fig. 2b).

### 2.2 Body wave traveltimes

We use three sets of traveltime data that were measured at a dominant period of ∼20 s and compiled by Kustowski *et al.* (2008). The first subset of arrival times was collected by Liu & Dziewoński (1998) from the seismograms of 1000 earthquakes ($M_W \geq 5.5$) of the period 1989–1994. The traveltime residuals were measured by cross-correlation of the observed and synthetic seismograms from PREM (Dziewoński & Anderson 1981). This set includes absolute traveltimes of phases *S, SS, ScS* and *ScSScS* as well as differential traveltimes of two phases such as *S–SKS* and *SKS–SKKS*. The second subset of arrival times, measured at Scripps by Woodward & Masters (1991) and Bolton & Masters (2001), includes differential *ScS–S* and *SS–S* traveltimes. Since the Scripps data used a different technique involving cross-correlation of the observed *ScS* or Hilbert-transformed *SS* waveform with the *S*-wave part of the seismogram, Kustowski *et al.* (2008) performed several checks for consistency between the data collected by the two groups. They concluded that the *ScS–S* data sets from Scripps and Harvard were consistent with each other. A constant correction of 1.1 s needs

**Table 2.** Data used in this study. Body wave traveltimes indicated by HRV were measured at Harvard, those indicated by SC at Scripps. The sources of the splitting functions are abbreviated as follows: Resovsky & Ritzwoller (1998) as R&R and Deuss *et al.* (2011) as D11.

| Data from Kustowski *et al.* (2008) | |
|---|---|
| | No. of surface wave phase anomalies |
| Love waves $T = 35$–$150$ s | 55 510–83 904 |
| Rayleigh waves $T = 35$–$150$ s | 160 470–206 560 |
| | No. of long-period waveforms |
| Body waves $T > 50$ s | 19 117–22 522 |
| Mantle waves $T > 125$ s | 16 440–24 101 |
| Mantle waves $T > 200$ s | 939–1062 |
| | No. of body wave traveltimes |
| S (HRV) | 27 660 |
| SS (HRV) | 11 695 |
| ScS (HRV) | 4397 |
| ScSScS (HRV) | 1279 |
| SS-S (HRV) | 5671 |
| SS-S (SC) | 16 180 |
| ScS-S (HRV) | 3471 |
| ScS-S (SC) | 7902 |
| S-SKS (HRV) | 3671 |
| SKKS-SKS (HRV) | 2232 |
| SS-S410S (HRV) | 18 677 |
| SS-S650S (HRV) | 18 670 |
| S410S-S650S (HRV) | 16 957 |
| Mode-splitting data | |
| | Source (No. of modes, splitting coefficients) |
| Spheroidal fundamentals | R&R (18, 1191) |
| | D11 (18, 1278) |
| Spheroidal overtones | R&R (28, 714) |
| | D11 (30, 1555) |
| Toroidal fundamentals | R&R (18, 522) |
| Toroidal overtones | R&R (11, 118) |

to be added to Scripps's *SS*–*S* data to account for a systematic difference of ∼1.1 s between the two sources of data. We adopt the same corrections to these data before including them in our inversions. The third data set consists of $SS$–$S_{410}S$, $SS$–$S_{650}S$ and $S_{410}S$–$S_{650}S$ differential traveltimes collected by Gu & Dziewoński (2002) and Gu *et al.* (2003) that provide constraints on the topography of the transition-zone discontinuities.

We relate these observations to the mantle elastic structure as well as the topography of transition-zone discontinuities (e.g. Gu *et al.* 2001; Kustowski *et al.* 2008). The general form of the equation governing the forward model of traveltime anomalies $\delta t$ to the properties of the Earth is written as

$$\delta t = -\int_{\text{path}} \frac{\sum_{i=1}^{5} \delta m_i T_{m_i}}{(v_0^{\text{group}})^2}\,\mathrm{d}s + \sum_{d_{410}} T_{410}\delta h_{410} + \sum_{d_{650}} T_{650}\delta h_{650}, \qquad (5)$$

where $d_{410}$ and $d_{650}$ denote interactions of the ray with the discontinuities, while $m_i$ stands for $v_{\text{PH}}$, $v_{\text{PV}}$, $v_{\text{SH}}$, $v_{\text{SV}}$ and $\eta$. The discontinuity kernels $T_{410}$ and $T_{650}$ are calculated using the expressions from Dziewoński & Gilbert (1976), while the kernels for elastic perturbations $T_{m_i}$ and group velocities $v_0^{\text{group}}$ are calculated using expressions from Kustowski *et al.* (2008) in their appendix. The ray paths are calculated using the expressions from Woodhouse (1981) for the 1-D reference model STW105 (Kustowski *et al.* 2008), while excluding its water layer.

### 2.3 Surface wave dispersion

We use the compilation of phase anomalies from Kustowski *et al.* (2008) that includes measurements of fundamental-mode Rayleigh and Love waves at nine periods between 35 and 150 s. The phase anomalies were collected from seismograms of the GSN and additional FDSN stations over the period 1992–2001 using the technique developed by Ekström *et al.* (1997). This technique is based on phase-matched filter theory and suppresses the interference of overtones using a minimization scheme for the residual dispersion. The expansion of the original data set was performed by Kustowski *et al.* (2008) to achieve a crossing of more than 200 rays in every 1000 km × 1000 km region on the Earth's surface. Owing to this excellent coverage, the uppermost mantle is well sampled globally by these surface wave data.

The linearized relation between the surface wave phase anomalies $\delta\Phi$ and the Earth's structure is given as

$$\delta\Phi = -\frac{\omega}{c_0}\int_{\text{path}} \frac{\delta c}{c_0}\,\mathrm{d}s, \qquad (6)$$

where $\delta c$ is the local phase velocity anomaly and $c_0$ is the phase velocity of the reference model. The perturbation in phase velocity at a fixed frequency $\omega$ is related to the perturbation in local eigenfrequency at a fixed wavenumber $k$ as $(\delta c/c)_\omega = (c/U)(\delta\omega/\omega)_k$ (Dahlen & Tromp 1998), where $U$ is the group velocity. The local

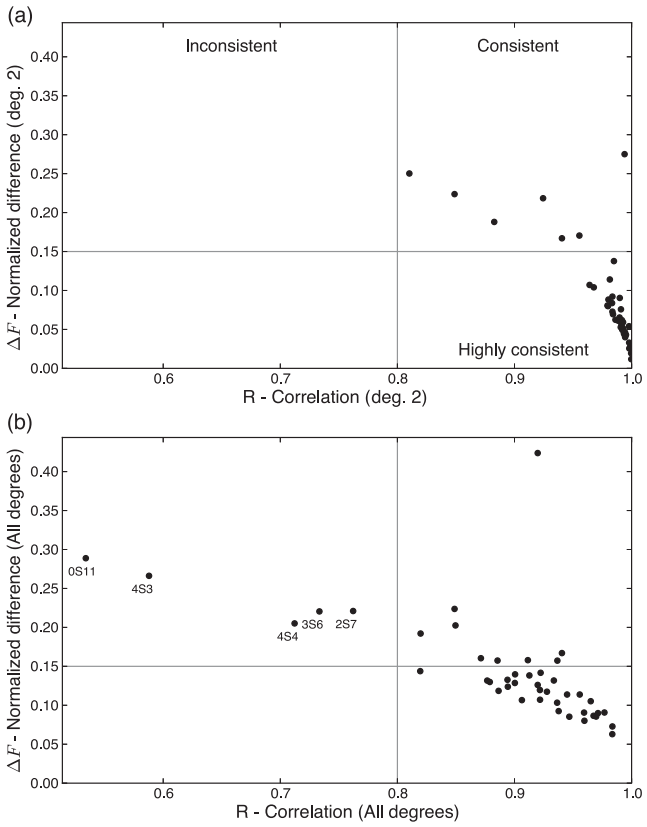


**Figure 2.** The consistency between the modes common to the two catalogues of splitting coefficients used in this study (Resovsky & Ritzwoller 1998; Deuss *et al.* 2011). The horizontal and vertical grey lines correspond to a normalized difference $\triangle F$, as in eq. (4), of 0.15 and correlation of 0.8, respectively. The calculations are truncated at (a) degree 2 or done for the (b) maximum degree available in the catalogues. The number of modes in the 'Inconsistent', 'Consistent' and 'Highly consistent' quadrants of each figure are the following: (a) 0, 7, 37 and (b) 5, 9, 30.

eigenfrequency perturbation is defined as

$$\delta\omega = \int_0^a \sum_{i=1}^{6} \delta m_i K_{m_i}\, \mathrm{d}r + K_{410}\delta h_{410} + K_{650}\delta h_{650}, \tag{7}$$

where the limits on the integration as well as the parameters $m_i$ are defined for a transversely isotropic earth model like in eq. (1). The kernels are computed from the eigenfunctions of normal modes in the 1-D reference model STW105 (Kustowski *et al.* 2008), using expressions from Takeuchi & Saito (1998) and Dahlen & Tromp (1998). These kernels are equivalent to the degree-0 kernels for mode-splitting functions ($K^0_{m_i}$) in eq. (1).

### 2.4 Mantle and body wave waveforms

The waveform data are taken from the compilation of Kustowski *et al.* (2008) and include seismograms from the years 1994–2003 of 219 well-recorded earthquakes ($M_W$ 6.5–8) and 10 great earthquakes ($M_W > 8$). The waveform fitting is restricted to very-long periods ($T > 200$ s) for the great earthquakes. A good coverage is obtained by selecting globally either the best-recorded events or earthquakes with different depths or magnitudes.

A seismogram recorded at station $r$ at location $\mathbf{x}_r$ for the $s$th earthquake is a function of time $t$, and can be expressed as

$$U_i(t) = u_i(\mathbf{x}_r, t, i_r, \mathbf{x}_s, t_s, \mathbf{f}_s, \oplus) + \varepsilon_i(t), \tag{8}$$

where the $i$th observed seismogram $U_i$ and the synthetic seismogram $u_i$ are recorded and calculated for the $s$th source and $r$th receiver, and $\varepsilon_i$ is the misfit. We assume that the receiver location $\mathbf{x}_r$ and the instrument response $i_r$ are known. The earthquake is characterized by a point source at location $\mathbf{x}_s$, origin time $t_s$, and the moment tensor $\mathbf{f}_s$. The goal of the waveform inversion is to find the source parameters and the perturbation $\delta\oplus$ that minimize the misfit

$$\varepsilon^2 = \sum_i \int_{\text{time}} \varepsilon_i^2(t)\, \mathrm{d}t = \sum_i \int_{\text{time}} [U_i(t) - u_i(t)]^2\, \mathrm{d}t \tag{9}$$

between observed seismograms $U_i$ and seismograms $u_i$ predicted by the model $\oplus$. Seismogram $u_i$ depends nonlinearly on the heterogeneous velocity field, and therefore, determination of the Earth's structure requires iterations. Starting with the standard Centroid Moment Tensor solutions (Dziewoński *et al.* 1981; Dziewoński & Woodhouse 1983), we invert iteratively for the aspherical perturbation $\delta\oplus$, the moment tensors $\mathbf{f}_s$ and centroid locations $\mathbf{x}_s$ and times $t_s$.

We use the path-average approximation (Woodhouse & Dziewoński 1984) to invert the waveforms for structure. The waveforms are constructed by the superposition of normal modes, while the sensitivity of the local eigenfrequency of a mode to the underlying structure is computed using eq. (7). More sophisticated numerical (e.g. Komatitsch & Tromp 2002a,b; Liu & Tromp 2008) and normal-mode approaches (e.g. Li & Romanowicz 1995) have been developed to calculate sensitivity kernels corresponding to 3-D models at global scales. Here, we follow the classical approach from Woodhouse & Dziewoński (1984) as this allows for a very efficient calculation of synthetic seismograms in aspherical earth models.

## 3 METHODS

### 3.1 Crustal corrections

Since the crust is very heterogeneous in terms of its velocity, density and thickness, appropriate corrections have to be made to the observations in Table 2 before inverting for mantle structure, as the long-period data used in our analyses cannot resolve the details of the crustal structure. In this study, the crustal effects are accounted for using the global model CRUST2.0 (Bassin *et al.* 2000). Here, we first summarize the techniques of crustal corrections for the body waves, surface waves and long-period waveforms that were used in developing the 3-D anisotropic model S362ANI (Kustowski *et al.* 2008). We then describe a new method of corrections for the mode-splitting data that uses the lateral variations of different discontinuities and heterogeneities, as represented in CRUST2.0, rather than using the variations in crustal thickness as in most earlier mode studies.

The corrections to the body wave traveltimes are calculated beneath the seismic stations, at points of surface reflection and at hypocentres of shallow earthquakes, employing a method based on ray theory, as described by Kustowski (2007). This procedure involves calculating time delays in a three-layer stratified medium with a local velocity structure as defined by CRUST2.0. Our simple ray-based approach differs from that of Ritsema *et al.* (2009) who accounted for the finite-frequency effects of body waves at

low frequencies by calculating the crustal time delay using cross-correlations of the waveform synthetics from PREM and the local crustal structure. Ritsema *et al.* (2010) used finite-frequency corrections to solve for the isotropic-velocity variations in their model S40RTS. However, experiments suggest that the recovered long-wavelength (>2000 km) structures are similar when either the finite-frequency or the ray-theoretical corrections are adopted (Ritsema *et al.* 2009). For simplicity, and since we focus on the long-wavelength mantle structure, we do not account for the finite-frequency effects while correcting for the crust in the traveltime data.

The corrections for the surface wave dispersion data are implemented by accumulating along the event–station ray path the difference in local phase velocity of the reference model (e.g. STW105) and that of the reference model overlain by the local crustal structure. We use the accumulated average phase velocity perturbation to calculate the crustal contribution to the phase anomaly with eq. (6). We then subtract this crustal contribution from the observed phase anomaly and use the corrected measurement in our inversions for mantle structure.

Application of an analogous method for the long-period waveforms would require calculating the total eigenfrequency perturbation along a ray path for the large number of modes (∼5000) that are typically required for calculating synthetic waveforms to the shortest periods (∼40 s). A linear-perturbation approach is therefore needed. However, at shorter periods, the non-linear effects from the strong lateral variations in the crust can be significant. Recent shear velocity models that employ long-period waveforms have used new techniques of calculating the crustal corrections that are computationally efficient yet account for the non-linear effects of the crust (Kustowski *et al.* 2007; Lekić *et al.* 2010). These non-linear effects, if neglected, can bias the results from tomographic inversions in certain regions of the Earth's mantle. Kustowski *et al.* (2007) found, for example, that the use of linear approximations (Woodhouse & Dziewoński 1984) in lieu of non-linear corrections led to overestimated fast-velocity anomalies in the mantle beneath cratons. We therefore use the method described in Kustowski *et al.* (2007) to calculate crustal corrections to the waveform data and develop a consistent method for the mode-splitting data, as described below.

Our new method of calculating the crustal splitting functions uses the spherical harmonic expansions of the discontinuities and heterogeneities used in the linear part of the corrections for the waveforms (Kustowski *et al.* 2007, eq. 2). The equivalent crustal splitting coefficient of a specified degree $s$ and order $t$ can be calculated using the expression

$$c_{st,\mathrm{crust}} = \sum_{i=1}^{3} \int_{\mathrm{Moho}}^{a} \left[ \delta v_S^{st,(i)} K_v^{s,(i)} + \delta \rho^{st,(i)} K_\rho^{s,(i)} \right] \mathrm{d}r + \sum_{j=1}^{5} K_j^s \delta h_j^{st}, \tag{10}$$

where the integral is taken over the radius $r$ from the Mohorovičić discontinuity (hereafter Moho) at a depth of 24.4 km to the free surface at $a = 6371$ km. Here, $v_S^{st}$, $\rho^{st}$ and $h^{st}$ stand for perturbations in shear wave velocities, density and topographies of crustal discontinuities, respectively. Also, $i = 1$, 2 and 3 correspond to the lower, middle and upper crust, and $j = 1, 2, \ldots, 5$ to the top of the mantle, upper crust, middle crust, lower crust and the ocean layer, respectively. We use a similar convention to the one used by Kustowski *et al.* (2007) where the 'upper crust' combines the upper crust, sediments and ice layers from CRUST2.0. We reduce the number of perturbations by adding the partial derivatives with scaling such that, $K_v^{s,(i)} = K_{v_S}^{s,(i)} + 0.8\, K_{v_P}^{s,(i)}$ since $v_S$ is strongly correlated with $v_P$ in CRUST2.0. We account for the density variations only in the upper crust in eq. (10), and therefore use five discontinuity corrections and four heterogeneity corrections, consistent with the waveform corrections that were used in constructing S362ANI (Kustowski *et al.* 2008).

**Table 3.** Crustal model used for the corrections to the splitting data. The crustal corrections are evaluated by calculating the perturbations to this model, expanded in spherical harmonics. The parameters $v_P$, $v_S$, $\rho$ and $h$ indicate compressional and shear velocities, density and thickness, respectively. The designation 'upper crust' combines the upper crust, sediments and ice layers from CRUST2.0

| Layer | $v_P$ [km s$^{-1}$] | $v_S$ [km s$^{-1}$] | $\rho$ [g/cm$^3$] | $h$ [km] |
|---|---|---|---|---|
| Ocean | 1.45 | 0.0 | 1.02 | 3.0 |
| Upper crust | 5.1 | 2.8 | 2.7 | 7.9 |
| Middle crust | 6.5 | 3.7 | 2.9 | 7.0 |
| Lower crust | 7.1 | 3.9 | 3.0 | 6.5 |

The calculations of the sensitivity kernels as well as the spherical harmonic expansions of the parameters in eq. (10) require a 1-D model. We overlay the spherical average of CRUST2.0 on top of the 1-D reference model STW105, while scaling the thicknesses of the upper, middle and lower crust such that the total thickness of the solid crust is the same as in PREM and STW105 (21.4 km). We also select the properties of the water layer to be the same as in PREM and STW105. The resultant 1-D model (Table 3) has three layers in the solid crust instead of the two layers in PREM and the partial derivatives $K_v^{s,(i)}$ and $K_\rho^{s,(i)}$ for degree $s$ can then be calculated using the expressions in eq. (1). The perturbations in shear wave velocities $v_S^{st,(i)}$, density $\rho^{st,(i)}$ and discontinuity depths $h_j^{st}$ describe, in spherical harmonics of degree $s$ and order $t$, the difference between the local structure in CRUST2.0 and the 1-D model obtained above. The new corrections for the splitting data, described here, are different from the corrections employed in previous mode studies that use only the crustal thickness in an approach similar to Woodhouse & Dziewoński (1984). The differences are small when compared with the signal from mantle heterogeneity, and inversions for the long-wavelength mantle structure give similar results with either scheme. Nevertheless, the new method used in this study is more consistent with the non-linear corrections employed for our long-period waveforms.

### 3.2 Parametrization and inversion

The reference model $[m_k^0(r)]$ in our study is the 1-D model STW105 and we invert for perturbations from it at various depths, defined as

$$\frac{\delta m_k(r,\theta,\phi)}{m_k^0(r)} = \sum_i \sum_j c_{ij} B_i(r) S_j(\theta,\phi), \tag{11}$$

where $m_k$ stands for the two parameters of interest, isotropic shear velocity and radial anisotropy in the mantle. Here, $c_{ij}$ is the coefficient of the model corresponding to the $i$th radial basis function $B_i$ and the $j$th lateral basis function $S_j(\theta, \phi)$. We describe the radial basis functions in terms of cubic B-splines (Lancaster & Salkauskas 1986) and the lateral basis functions in terms of 362 evenly spaced spherical splines (e.g. Wang & Dahlen 1995), as shown in Fig. 3. We parametrize the shear velocity model in terms

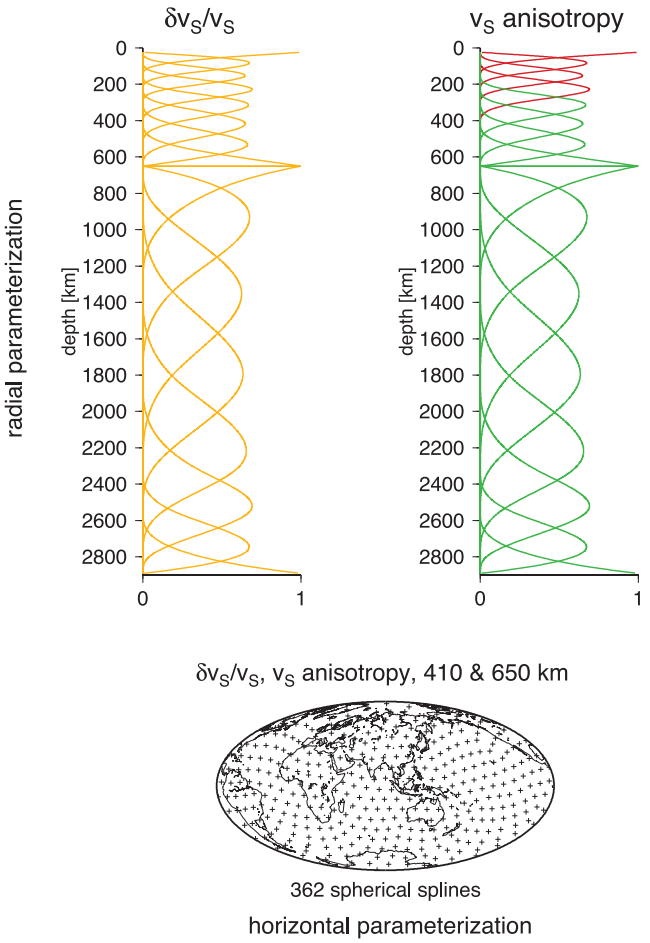


**Figure 3.** The 3-D parametrization of the mantle used in this study. Shown in yellow are the 16 cubic splines used to describe vertical variations in isotropic shear velocities. The top four cubic splines are first used to describe the anisotropy in the upper mantle (red) and 12 more are added at depth (green) to test the resolution of whole-mantle anisotropy by our data set. Pluses indicate knots of 362 spherical splines used to describe lateral variations in shear wave velocity, anisotropy and the topographies of the 410- and 650-km discontinuities.

of isotropic and anisotropic variations as

$$\frac{\delta v_S}{v_S^0} = \frac{\frac{\delta v_{SH}}{v_{SH}^0} + \frac{\delta v_{SV}}{v_{SV}^0}}{2} \quad \text{and} \quad \delta a_S = \frac{\delta v_{SH}}{v_{SH}^0} - \frac{\delta v_{SV}}{v_{SV}^0}, \tag{12}$$

and also solve for the 2-D topography of the 410- and 650-km discontinuities. This parametrization scheme allows us to regularize independently the roughness of isotropic and anisotropic velocity variations. Since the mode-splitting data are provided in terms of even-degree spherical harmonics, we use a projection matrix to convert the spline coefficients in the model to spherical harmonic coefficients, as described in the Appendix.

The model coefficients $c_{ij}$ correspond to a finite number of basis functions and we apply discrete inverse theory (e.g. Menke 1989) to solve the inverse problem. We write the problem as the solution to the least-squares inverse problem $x_{LS} = (A^T A)^{-1}(A^T d)$, where $x_{LS}$ is a matrix containing the best-fitting model coefficients $c_{ij}$. Here, $d$ corresponds to the data and $A$ to their sensitivity to the perturbations in $c_{ij}$ using the kernels described in Section 2, weighted according to the uncertainties in the measurements. Due to imperfect data coverage and measurement errors, and in order to stabilize the inversion, we regularize the tomographic inversions by minimizing vertical and horizontal gradients. Since models regularized by norm damping have a tendency to correlate with uneven data coverage (Boschi & Dziewoński 1999), we choose not to minimize the norm of the solution in our inversions. The solution to the inverse problem is then modified to

$$x_{LS} = \left[\sum_i w_i (A^T A)_i + \sum_j d_j (D^T D)_j\right]^{-1} \left[\sum_i w_i (A^T d)_i\right], \tag{13}$$

where $w_i$ and $d_j$ are the weights given to various types of data and damping, respectively. Here, $i$ corresponds to the body wave traveltimes, surface wave phase anomalies, body and mantle waveforms, as well as the normal-mode splitting coefficients. Also, $j$ corresponds to vertical and horizontal gradients of the model (eq. 11) and $(D^T D)_j$ are the respective damping matrices, which are calculated numerically (e.g. Boschi & Dziewoński 1999; Gu *et al.* 2001; Kustowski *et al.* 2008).

We then calculate the weighted least-squares solution to eq. (13) using a standard Cholesky factorization for positive-definite matrices (e.g. Trefethen & Bau 1997). The weighting scheme for the body wave traveltimes, surface wave phase anomalies and long-period waveforms is kept the same as the one used for determining S362ANI (Kustowski *et al.* 2008). The relative weighting of the additional data sets of mode-splitting coefficients is decided in a way that maximizes their variance reductions without appreciably reducing the fit to the other types of data.

### 3.3 Starting model and integrated depth sensitivity

Our starting model consists of the 1-D reference model STW105 and the corresponding 3-D upper-mantle anisotropic model S362ANI from Kustowski *et al.* (2008). Since the sensitivity kernels for the long-period waveforms require a 3-D starting model, the combination of STW105 and S362ANI is used in that calculation. The sensitivity matrices for normal-mode splitting functions, body wave traveltimes and surface wave phase anomalies are calculated from the 1-D starting model STW105. We do not solve for lateral variations in density or the $\eta$ parameter, which controls the variation of compressional and shear velocities at intermediate incidence angles (Dziewoński & Anderson 1981). To reduce the number of free parameters, we scale the variations between compressional and shear velocities assuming that $\delta v_{PH}/v_{PH} = 0.55\,\delta v_{SH}/v_{SH}$ and $\delta v_{PV}/v_{PV} = 0.55\,\delta v_{SV}/v_{SV}$. The scaling factor of 0.55 is consistent with anomalies predicted from purely thermal effects (Karato 1993) and with the results from earlier tomographic studies of shear and compressional wave velocities in the mantle (e.g. Robertson & Woodhouse 1996). Moreover, petrological constraints (Montagner & Anderson 1989) suggest similar correlations between the compressional and shear wave velocities in the mantle. An analysis of the scaling ratios and their resolution with our data set is beyond the scope of this study.

The various data sets provide different depth-integrated sensitivity to velocity and anisotropy in the Earth's mantle. To illustrate this, we compute the global average of the diagonal elements of the weighted inner-product matrix $A^T A$ as a proxy for the sensitivity at the depth of the spline (Gu & Dziewoński 2002) and plot the values without any normalization (Kustowski *et al.* 2008) in Fig. 4. Compared with Kustowski *et al.* (2008), we also plot the sensitivities for the different types and sources of mode-splitting data. The upper mantle at depths down to 300 km is best constrained by

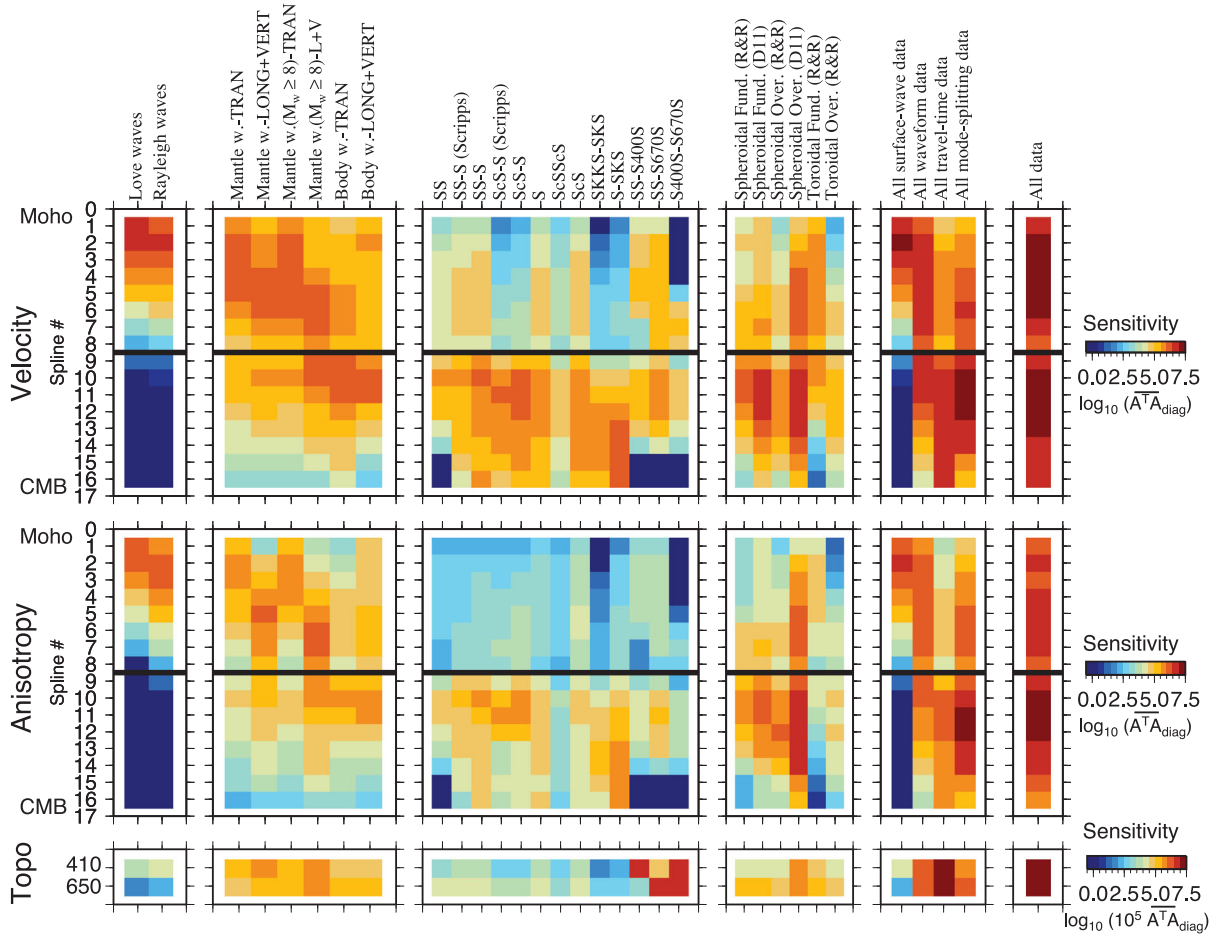


**Figure 4.** The sensitivity of different data sets is represented by the global average of the diagonal elements of the inner-product matrix $A^TA$ for every cubic spline and for the discontinuities in the transition zone. The $A^TA$ matrices are weighted in the same way as in the inversions. The panels on the right show cumulative sensitivities for the surface wave, waveform, traveltime and normal mode data, and for all data combined. LONG, TRAN and VERT indicate longitudinal, transverse and vertical components of a seismogram, and 'w.' denotes waveforms. The sources of the mode-splitting functions are indicated as follows: 'R&R' to Resovsky & Ritzwoller (1998) and 'D11' to (Deuss *et al.* 2011), while 'Fund.' and 'Over.' denote fundamental and overtone modes, respectively. Note the different scale for the topography sensitivities.

the fundamental-mode surface waves. Teleseismic body waves have peak sensitivity at the depth of their turning point in the lower mantle, but also sample the upper mantle beneath the sources, receivers and the points of reflection on the surface. The sensitivity to the structure in the transition zone is obtained from overtones, which are incorporated using the long-period waveforms and the overtone-mode-splitting data. The lowermost mantle is best sampled by horizontally polarized *S* waves diffracted at the core–mantle boundary, which are sensitive only to variations in $v_{SH}$. The *SKKS–SKS* and *S–SKS* differential traveltimes are sensitive to both $v_{SH}$ and $v_{SV}$ and we give these data large weights in the inversion, like in Kustowski *et al.* (2008), to constrain any anisotropic variations at the bottom of the mantle. Topography of the transition-zone discontinuities is determined primarily by traveltimes of *SS* precursors. Long-period waveforms also have significant sensitivity to perturbations in the depths of discontinuities.

## 4 RESULTS

We use the full data set to solve for three models of different complexity: S362ISO+M, which includes only isotropic perturbations, S362ANI+M, which includes radial anisotropy in the upper ~300 km like in S362ANI, and a whole-mantle anisotropic model, S362WMANI+M. The inversions parallel those performed by Kustowski *et al.* (2008) with the difference being the addition of the mode data sets. Key questions are then to what extent and how the models are changed as a result of including mode constraints, and the ability of the new models as well as the earlier ones to fit the different data sets. We first present the fits to the observations and then describe the resulting models in detail.

### 4.1 Fits to the data

Fig. 5 summarizes the fits obtained for the different data sets using the new models and S362ANI, the preferred model from Kustowski *et al.* (2008). All new models fit the mode-splitting data better than S362ANI. For example, the improvement in variance reduction from S362ANI to S362ANI+M is 13.6 per cent for the fundamental spheroidal mode data from Deuss *et al.* (2011). The fits to the three earlier data sets with the new models are very similar to those obtained with the corresponding ones by Kustowski *et al.* (2008). In particular, the model S362ANI+M provides essentially the same fits to the other data sets as S362ANI. It should be noted that S362ANI does predict the mode-splitting data relatively well, with variance reductions in the range of ~65–75 per cent for the different subsets of data. Satisfactory fits by S362ANI, a model not constrained using

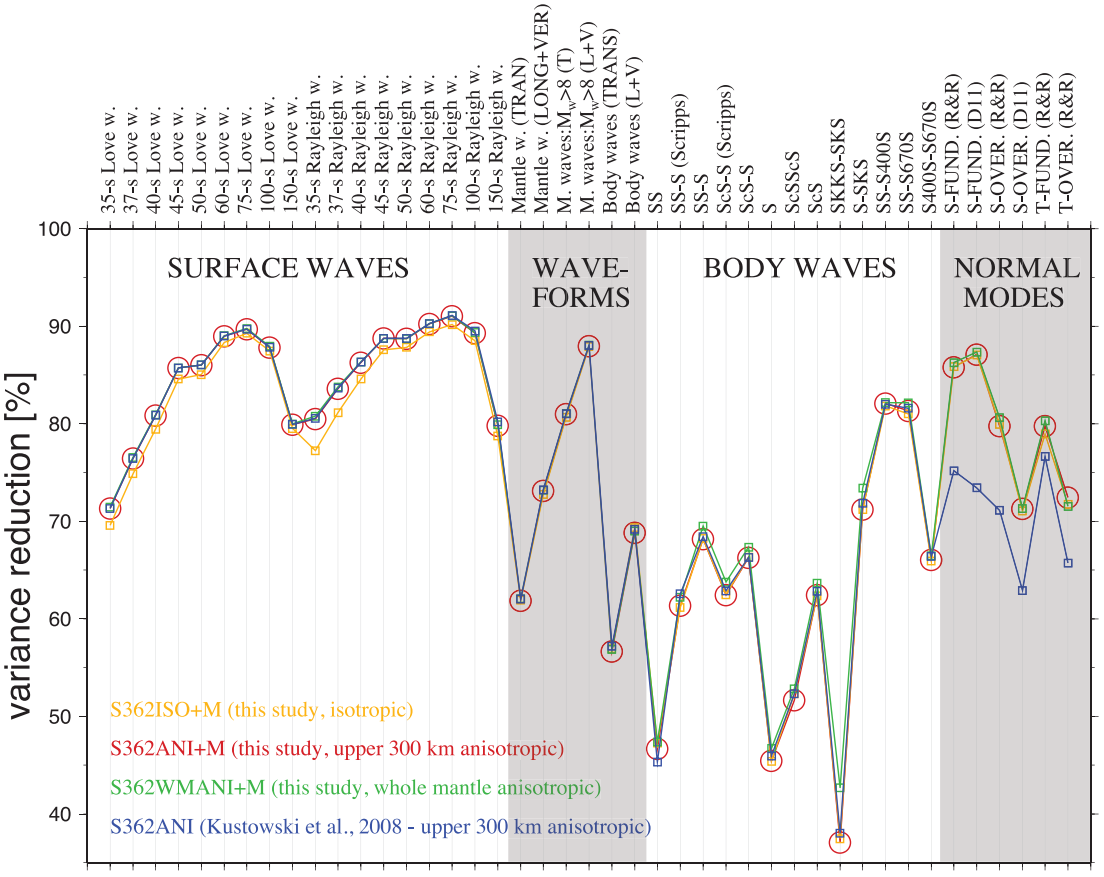


**Figure 5.** Variance reductions for the models in this study—whole-mantle anisotropic model S362WMANI+M (in green), S362ANI+M with anisotropy confined to the four uppermost splines (in red) and for the model S362ISO+M without lateral anisotropic variations (in yellow). S362ANI (Kustowski *et al.* 2008) was derived using all the data sets except the splitting functions ('NORMAL MODES'). The variance reduction was calculated separately for measurements of surface wave phase velocities at different periods, for different types of waveforms and different types of body wave traveltimes and normal-mode splitting functions. S-FUND and T-OVER refer to spheroidal fundamental modes and toroidal overtones, respectively.

mode-splitting data, can be attributed to the use of other data such as long-period waveforms that also provide some bulk constraints on long-wavelength mantle structure.

Since different modes have varying sensitivity to isotropic and anisotropic structure (Fig. 1), their fits with models of different anisotropic complexity (Fig. 5) help clarify how well the heterogeneity is constrained by the data. We observe, consistent with Kustowski *et al.* (2008), that including anisotropy in the top 300 km of the upper mantle significantly improves the fit to the surface wave data, while whole-mantle anisotropy improves the fit to some traveltime data, especially *S–SKS* and *SKKS–SKS*. The improvements in fit to the mode-splitting observations upon adding anisotropy in the upper mantle is low, because the integrated sensitivity to elastic structure is small for such a limited range of depths. On solving for the whole-mantle anisotropic model, the splitting functions of spheroidal overtones ($_4S$ and $_6S$ branches) and the high-$l$ toroidal fundamentals (e.g. $_0T_{10}$ and $_0T_{14}$) show improvements in fit. However, such improvements are small and all three models—S362ISO+M, S362ANI+M and S362WMANI+M—provide similar fits to the mode-splitting observations. We focus on comparisons between the fits of S362ANI and S362ANI+M.

We quantify the fit between the observed and predicted splitting function by calculating the correlation ($R$) and normalized difference ($\triangle F$) for all available degrees. We cross-plot these values for each mode in Fig. 6, separately for the two catalogues (R&R, D11) and the models, S362ANI and S362ANI+M. We observe that S362ANI+M provides good fits ($\Delta F < 0.15$) to almost twice as many modes in each catalogue as S362ANI. In case of the D11 data, 40 modes out of 48 show good fits with S362ANI+M in contrast to only 23 with S362ANI. The improvements in fit are also observed to a lesser extent for the R&R data; S362ANI+M provides good fits to 44 out of 75 modes compared to 26 with S362ANI. In general, the newer D11 data are fit better than the R&R data with our models. However, the R&R measurements for a few modes (e.g. $_1S_2$, $_0S_{11}$ and $_0S_{12}$) are more consistent with the predictions from S362ANI+M than their D11 counterparts.

Limitations of the data and the modelling scheme can be analysed by identifying modes not fit well by either S362ANI or S362ANI+M. The variance reductions for the splitting coefficients of each mode are calculated for the two models and plotted in Fig. 7. The spheroidal fundamental modes and the first overtone branch ($_1S$) show the largest improvement in fit with S362ANI+M. The upper-mantle-sensitive second-overtone branch ($_2S$) and the toroidal fundamental modes show modest improvements in fit since S362ANI was already constrained well in the upper mantle. Some modes that are difficult to measure do not show appreciable improvements in fit from S362ANI to S362ANI+M. The fundamental mode $_0S_{11}$, for example, cross-couples with the toroidal mode $_0T_{12}$ due to the Coriolis force; such effects complicate the estimation of self-coupled splitting coefficients for either mode (Resovsky & Ritzwoller 1999b). The mode $_0S_2$ is only modestly fit with S362ANI+M, which may be due to its sensitivity to density that is not modelled in

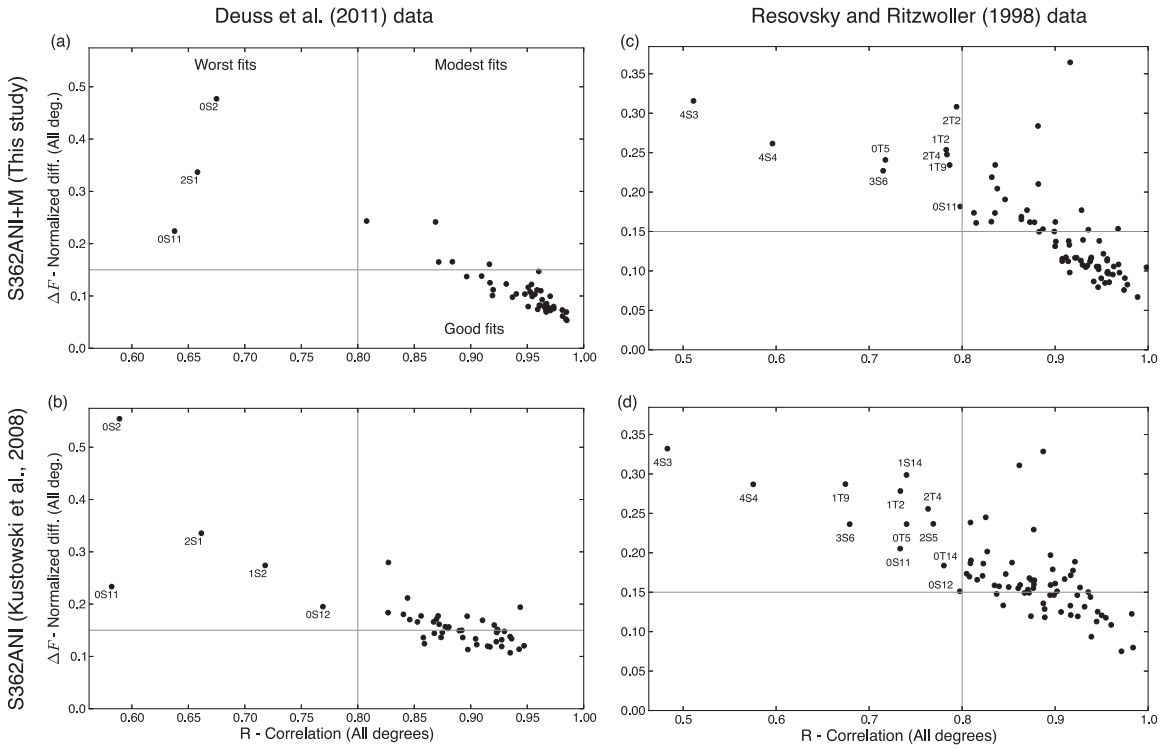


**Figure 6.** The fits from the models S362ANI+M (this study) and S362ANI to the two catalogues of splitting coefficients used in this study (Resovsky & Ritzwoller 1998; Deuss *et al.* 2011). The horizontal and vertical grey lines correspond to a normalized difference $\Delta F$, as in eq. (4), of 0.15 and correlation of 0.8, respectively. The number of modes in the 'Worst fits', 'Modest fits' and 'Good fits' quadrants of each figure are the following: (a) 3, 5, 40, (b) 5, 20, 23, (c) 9, 22, 44 and (d) 12, 37, 26. The calculations are truncated at the maximum degree available in the catalogues.

this study. S362ANI+M does not provide a good fit to the mode ${}_1S_2$ from the D11 catalogue. The measurements for ${}_1S_2$ are inconsistent amongst various studies and this mode has some sensitivity to the inner core (Deuss *et al.* 2011); it is unclear what explains our low fits. The reasons for the modest fit to ${}_2S_1$ are also unclear. Other mantle models constrained using mode-splitting data, such as S20RTS, also do not show good fits for this mode (Deuss *et al.* 2011).

A visual comparison of the observed splitting functions of some representative modes with those predicted by S362ANI and our model S362ANI+M is presented in Fig. 8. S362ANI+M gives better fits to the splitting functions of lower-mantle-sensitive modes, such as ${}_0S_9$ and ${}_1S_8$, especially at high latitudes. The data for the high-$l$ toroidal fundamental modes such as ${}_0T_{10}$, and some toroidal overtones such as ${}_1T_9$, which have sensitivity in the transition zone (Fig. 1), are also fit better with S362ANI+M than S362ANI. However, the amplitudes of the toroidal-mode-splitting functions are not fit well by either model. S362ANI+M provides better fits than S362ANI to the splitting data of all but four modes: ${}_0S_7$, ${}_3S_9$, ${}_0T_5$ and ${}_2T_2$ (Fig. 7). The spheroidal modes ${}_0S_7$ and ${}_3S_9$ are only slightly worse fit by S362ANI+M with variance reductions of around 81 per cent from both models. The variance reductions for the toroidal modes ${}_0T_5$ and ${}_2T_2$ are low (<56 per cent) for both models.

### 4.2 Isotropic shear velocity

The isotropic shear velocity variations in the mantle, as represented by S362ANI+M, are compared to the model S362ANI (Kustowski *et al.* 2008) in Fig. 9. At a depth of 50 km, the pattern of heterogeneity in S362ANI+M is similar to S362ANI and is dominated by strong negative anomalies that are aligned with mid-ocean ridges and regions of backarc extension. Other upper-mantle features in S362ANI, such as mid-ocean ridge signatures down to at least 150-km depth and strong positive anomalies at 150 km beneath continents, are also seen in S362ANI+M. Most of the differences between the isotropic parts of the models arise at depths below 300 km. In the transition zone, the differences between the models are in the range of one-fourth of the anomalies themselves with generally stronger heterogeneity in the new model. The correlation between the models does not decrease below ~0.8 even in the transition zone and the mid-mantle where differences are the most substantial, indicating that the patterns of isotropic heterogeneity are robust (Fig. 10a).

The faster-than-average velocities associated with major subduction zones that reach up to +3 per cent anomalies in the transition zone nearly vanish in the mid-mantle. This change in heterogeneity is readily observed in the root-mean-square (rms) variations of the two models (Fig. 10b). S362ANI+M shows a more abrupt change across the 650-km boundary than S362ANI. The degree-2 anomalies in the transition zone, associated with subducted slabs in the circum-Pacific, are stronger in power with the new model that includes mode data. In the lowermost mantle, S362ANI+M is dominated by large-scale slow-velocity superplumes beneath the Pacific and Africa. These anomalies are as low as –3.5 per cent slower than average. S362ANI+M shows a Pacific superplume that is more laterally focused than in S362ANI, while the amplitude of the imaged superplume beneath Africa is weaker by ~0.9 per cent (Fig. 9). This slight reduction in power of the isotropic anomalies in the lowermost mantle is primarily in the long-wavelength (degree-2) variations (Fig. 10b).

The differences in isotropic structure in the mid-to-lower mantle are primarily restricted to the Southern Hemisphere (Figs 9 and 10c),

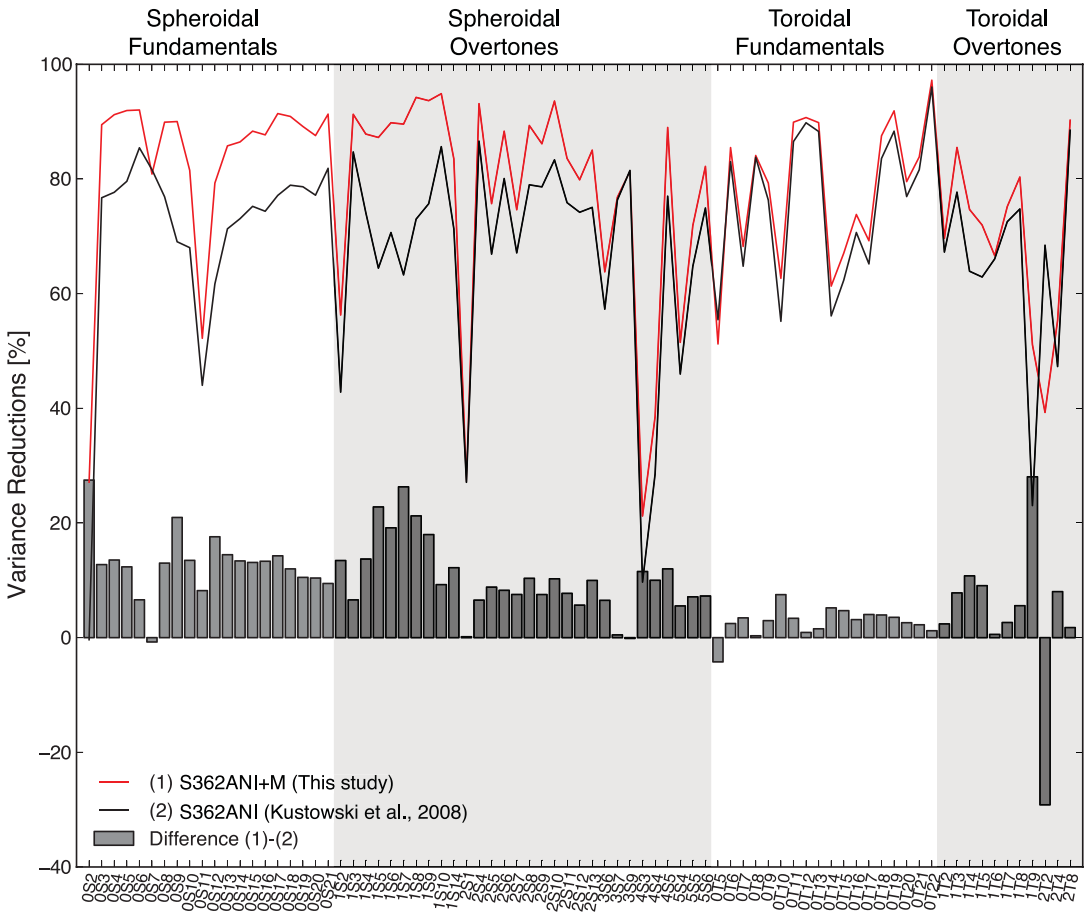


**Figure 7.** The variance reductions for the splitting coefficients for each mode are calculated for the two models S362ANI+M (this study) and S362ANI. The coefficients from both the catalogues (Resovsky & Ritzwoller 1998; Deuss *et al.* 2011) are used while computing the variance reduction for a common mode. The predictions include the crustal contribution to the splitting functions from our new method using CRUST2.0.

while the differences are globally distributed in the transition zone (Fig. 10b). Owing to the global large-scale sampling of the mode-splitting functions, they are less influenced by the distribution of earthquakes and stations than other types of data. The ray coverage of traveltime data is limited in the Southern Hemisphere due to the denser distribution of stations on the continents. Our analysis also indicates that the additional heterogeneity in S362ANI+M, compared to S362ANI, is primarily in the low even-degree variations (up to degree 8). Although other data such as the long-period waveforms provide some constraints on large-scale variations, the mode-splitting data used in S362ANI+M provide more direct constraints on the even-degree structure.

### 4.3 Comparison of isotropic velocity with other studies

A common way of assessing the resolution of model parameters in a least-squares inversion is through its resolution matrix (e.g. Menke 1989). Such resolution tests for the shear velocities in the mantle and topographies of the transition-zone discontinuities performed by various authors (e.g. Gu *et al.* 2003; Panning & Romanowicz 2006) indicate that large-scale structures in the mantle can be recovered. A quantitative comparison between tomographic models can also help distinguish stable features from those influenced more by data selection and other technical choices. We invert only for the large-scale variations (degree $\leq 16$) using a large compilation and with more types of data than used in earlier studies. Therefore, standard resolution tests on our specific modelling scheme will provide limited additional insights and we, instead, focus on examining the level of consistency in isotropic velocities across two generations ('pre-2008' versus 'recent') of shear velocity models that were derived from different modelling approaches.

The model S20RTS, a pre-2008 model (Ritsema *et al.* 1999), and its successor, S40RTS (Ritsema *et al.* 2010), were obtained from measurements of fundamental-mode and overtone surface wave velocities, body wave traveltimes and spheroidal-mode-splitting data, most of which are sensitive primarily to the $v_{SV}$ structure. S40RTS, the recent model, includes an order-of-magnitude larger data set than S20RTS, uses crustal body wave traveltime corrections from long-period synthetic waveforms rather than from ray theory and solves for degree-40 rather than degree-20 variations in isotropic shear velocity. The second pre-2008 model, SAW642AN (Panning & Romanowicz 2006), and its successor, SAW642ANb (Panning *et al.* 2010), were determined using three-component surface- and body wave waveforms using non-linear asymptotic mode-coupling theory. SAW642ANb, the recent model, was developed using a new method of non-linear crustal corrections compared to SAW642AN. Fig. 11 shows the correlations between the isotropic parts of S362ANI and S362ANI+M with these four models.

We observe that the correlations are higher between the recent generation of models (Figs 11c and d) than between the pre-2008 models (Figs 11a and b), especially in the lower mantle. Specifically, the correlation between S362ANI+M and S40RTS is greater

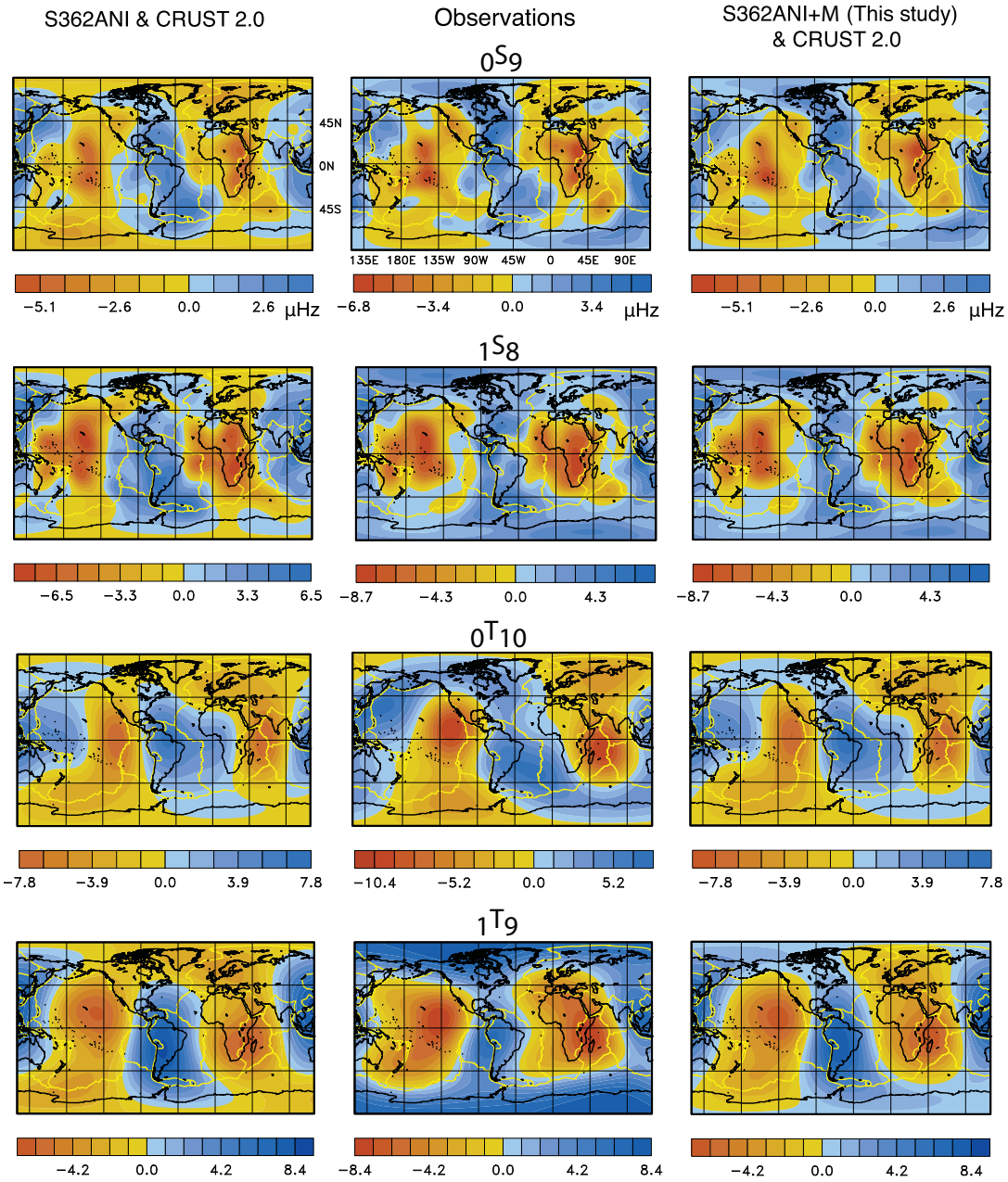


**Figure 8.** The fits to the observed splitting functions by S362ANI+M (this study) and S362ANI. The measured splitting functions of different spheroidal (Deuss *et al.* 2011) and toroidal (Resovsky & Ritzwoller 1998) modes are plotted in the middle column. The third column contains prediction from S362ANI+M and the crustal model CRUST2.0 while the first column contains that of S362ANI and CRUST2.0. The crustal splitting function is calculated using a new method (Section 3.1). All the splitting functions are in units of μHz.

than 0.60 at all depths in the mantle, except the shallow mid-mantle. The depth-averaged correlation in the whole mantle between the two models is 0.70, an improvement of 0.04 from S20RTS and S362ANI. The degree-2 variations in the transition zone are very well correlated between the two models. The correlations at shallower depths remain high ($R \sim 0.76$) and are almost the same between the two generations of models. The higher correlations in the transition zone and the mid-mantle for the recent models may be attributed to the inclusion of the mode-splitting functions from Deuss *et al.* (2011), which have been modelled by both S362ANI+M and S40RTS.

The correlations of SAW642ANb with the other recent models are lower in the transition zone and in the mid-mantle (Fig. 11d). SAW642ANb has whole-mantle correlations of 0.59 with S362ANI+M and of 0.63 to S40RTS, somewhat lower than the correlation between S362ANI+M and S40RTS ($R = 0.70$). Nevertheless, these correlations are higher by 0.04–0.06 than in the earlier generation of models. We observe a substantial increase in correlations from S362ANI and SAW642AN to S362ANI+M and SAW642ANb (Figs 11b–d), with lower-mantle average improvement of 0.08. Almost all of the improved agreement occurs on going from S362ANI and SAW642AN to S362ANI and SAW642ANb. We infer that this improvement results primarily from the implementation of the non-linear crustal corrections in SAW642ANb rather than from the inclusion of modes in S362ANI+M. The use of

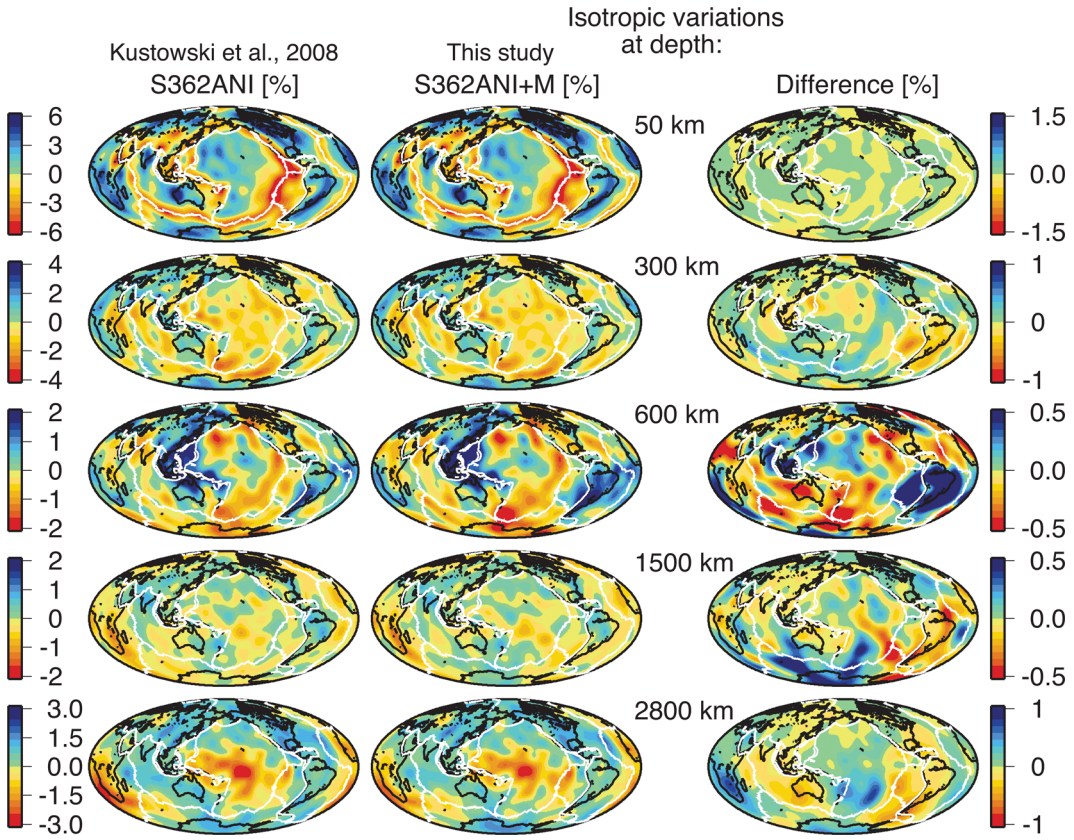


**Figure 9.** Isotropic shear wave velocity perturbations ($\delta v_S/v_S^0$) at 50, 300, 700, 1500 and 2800 km in S362ANI+M and S362ANI. The differences are shown on the right with a colour scale that is scaled 1/3 or 1/4 from the absolute variations.

mode-splitting functions in S362ANI+M gives an additional increase in correlations with SAW642ANb in the mid to lower mantle for degree-2 variations.

Although the overall level of agreement has increased in the recent generation, some features show exceptions to this trend. The degree-2 correlations at a depth of ∼250 km are low in the pre-2008 models and lower yet in the recent generation of models. Rapid radial changes in the heterogeneity occur at around 250-km depth, the details of which vary between models. The differences lead to low correlations over a narrow range of depths.

Another way to compare tomographic models at different wavelengths is through the analysis of their power spectra (Fig. 12). In the uppermost 200 km, the spectra of all recent models are dominated by the lowest 5–6 degrees representing strong anomalies of roughly continental size. In contrast, the power spectra are weaker and white at 250-km depth. All recent models show this abrupt change in the strength and dominant wavelength of heterogeneity at 200-km depth. Both S40RTS and S362ANI+M, like in the earlier generation of models, show a local maximum in the power of degree-2 anomalies in the transition zone. Amplitudes of the isotropic anomalies in this depth range are larger than in earlier models. The differences between the models can be explained, in part, by the split radial parametrization used in S362ANI+M, versus the continuous one used in S40RTS. SAW642ANb has lower power in its degree-2 component than SAW642AN at a depth of 600 km and does not show the abrupt change in the spectrum across the 650-km discontinuity observed in other recent models. The low correlations in the mid-mantle between S362ANI+M and SAW642ANb (Fig. 11) could also be due to the low power in SAW642ANb at degrees higher than five at this depth. The lower-mantle spectra are, in general, dominated by the well-correlated degree-2 superplumes; differences exist in the odd-degree variations.

### 4.4 Radial anisotropy

The anisotropy in S362ANI+M is restricted to the upper ∼300 km in the mantle and is almost identical to that in S362ANI. Therefore, we focus here on describing the whole-mantle anisotropic model S362WMANI+M. Fig. 13 shows the total rms values of anisotropic variations in the models S362WMANI+M and S362WMANI (Kustowski *et al.* 2008) and their intermodel correlations. The anisotropy in the shallowest ∼300 km of the mantle in S362WMANI+M is similar to that in the older model S362WMANI ($R > 0.95$; Fig. 13a), which was constrained well by surface wave dispersion and waveform data. The uppermost mantle is also the region of strongest radial anisotropy in the mantle with rms lateral variations of up to ∼1.3 per cent (Fig. 13b).

The consistency between anisotropic variations decreases at depths greater than 300 km. The correlations in anisotropy between S362WMANI and S362WMANI+M are slightly lower in the transition zone ($R \sim 0.85$) than in the uppermost mantle (Fig. 13a). The addition of modes results in marginally stronger rms lateral variations of anisotropy for the transition zone in S362WMANI+M than in S362WMANI (Fig. 13b). In the mid-mantle, the degree-2 variations are negatively correlated between S362WMANI and S362WMANI+M and total correlations are lower than 0.6 at some depths in the mid-mantle. Differences in anisotropic variations are not only in their patterns, as manifested by the intermodel correlations, but in their amplitudes as well. The rms values of anisotropic

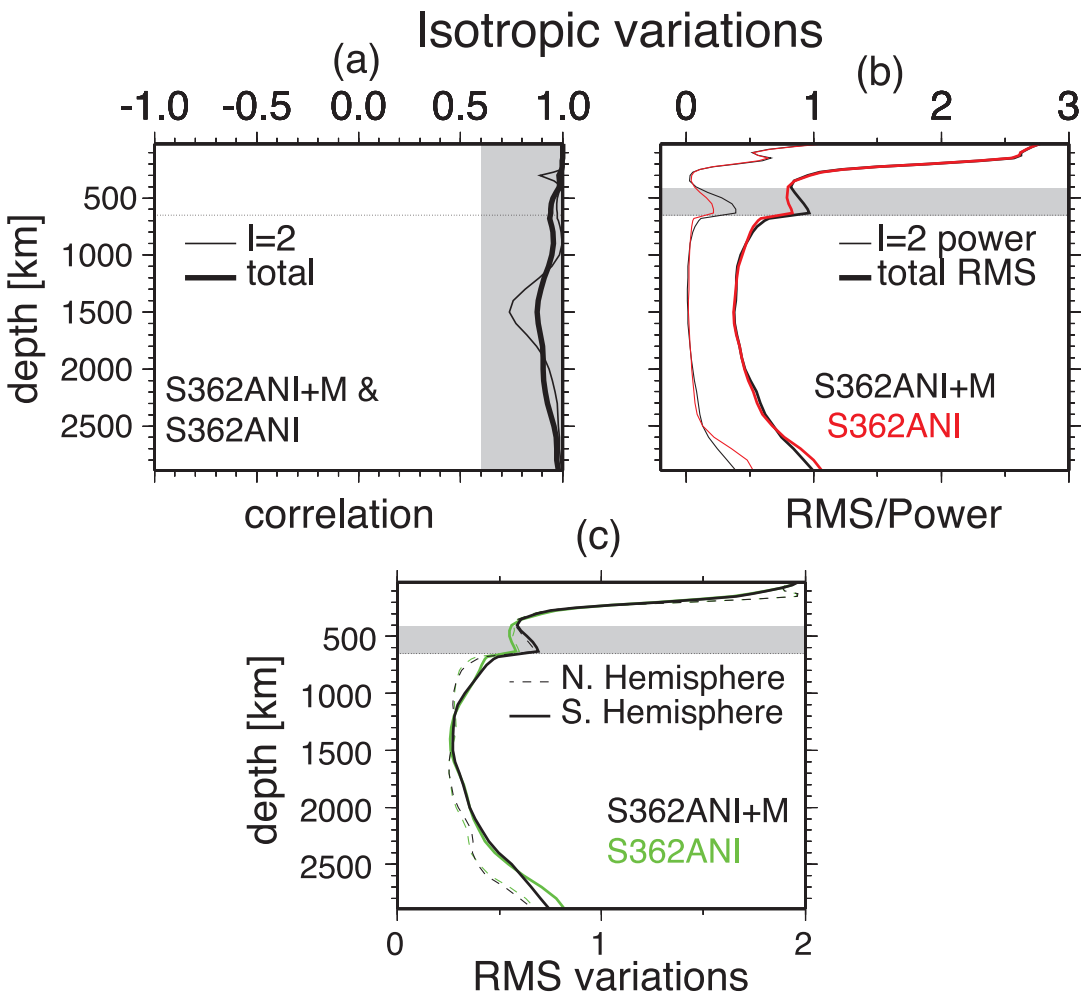


**Figure 10.** Comparisons between the isotropic parts ($\delta v_S/v_S^0$) of S362ANI+M and the earlier model S362ANI. (a) The correlations between the isotropic variations of the two models at degree 2 and for all degrees. (b) The power of degree-2 variations and the total root-mean-square (rms) values of isotropic shear velocities in the two models. (c) The power in degree 2 and rms values of heterogeneity in the two hemispheres for the two models.

variations in the mid-mantle are low in S362WMANI, and are smaller by ∼0.1 in S362WMANI+M. In the transition zone, the variations in S362WMANI+M exceed 3 per cent $v_{SH} > v_{SV}$ beneath North America and the Northwest Pacific and is ∼2 per cent $v_{SV} > v_{SH}$ beneath South America (Fig. 14a). Strong anisotropic variations in the lowermost mantle of up to 2 per cent $v_{SV} > v_{SH}$ are located beneath the Tonga-Kermadec and New Hebrides trenches. Strong localized anomalies of up to ∼3 per cent $v_{SH} > v_{SV}$ are also seen in the lowermost mantle beneath the Western Pacific, Alaska and the Caribbean.

We investigate the resolution of anisotropic variations in our models by comparing them with other studies. Our whole-mantle anisotropic model S362WMANI+M is compared with SAW642ANb, since S40RTS, as discussed in Section 4.2, is isotropic. At a depth of 150 km, both S362WMANI+M and SAW642ANb exhibit strong radial anisotropy with additional $v_{SH} > v_{SV}$ variations localized beneath the Pacific. However, the $v_{SH} > v_{SV}$ anisotropy beneath continents, reported by Gung *et al.* (2003), is less evident in S362WMANI+M. The uppermost and lowermost mantle are regions where the models S362WMANI+M and SAW642ANb are somewhat correlated (Fig. 14b). The low-amplitude anisotropic anomalies in the mid-mantle are poorly correlated between the two models. Unlike the previous generation of anisotropic models, the correlation in the lowermost mantle is as high as 0.8 for the degree-2 variations ($R_2$). The better agreement in degree-2 anisotropic variations holds promise for resolving the debate on the presence of large-scale anisotropy in the lowermost mantle. However, it should be noted that the spectra of anisotropic heterogeneities in the deep mantle are not dominated by degree-2 anomalies unlike those of the isotropic heterogeneities (Section 4.5, Figs 16a and b). Therefore, too much emphasis should not be placed on such agreements, especially because anisotropic features in the deep mantle are not unambiguously required to fit the data (Fig. 5). Apart from the differences in spectral content, anisotropic features are also spatially uncorrelated with isotropic anomalies in both SAW642ANb and S362WMANI+M ($-0.3 < R < 0.3$, Fig. 14c).

### 4.5 Importance of inverting multiple data types

The additional constraints on mantle structure afforded by mode-splitting observations are illustrated by comparing the data fits for the two anisotropic models from Kustowski *et al.* (2008), S362ANI and S362WMANI, with those of S362ANI+M (Fig. 15). It is noteworthy that the model S362WMANI, which was developed together with S362ANI but allowed for radial anisotropy throughout the mantle, provides worse fits to the mode data than either S362ANI

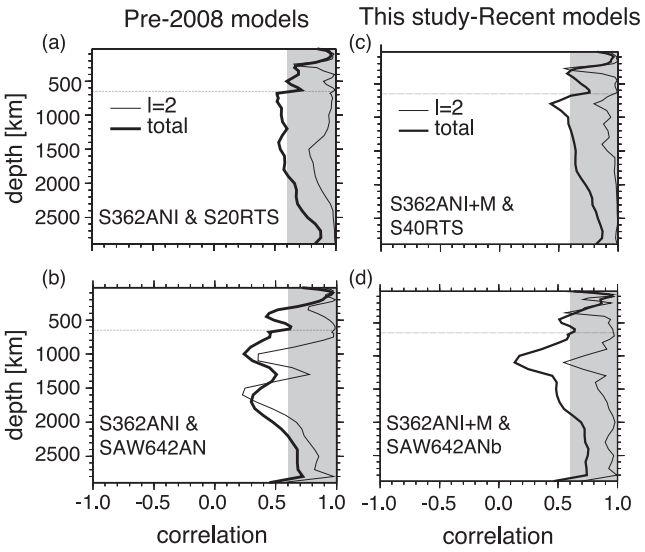


**Figure 11.** Correlation between the isotropic shear velocities in the recent (right) and earlier (left) generation of models. S40RTS is a degree-40 isotropic shear velocity model (Ritsema *et al.* 2010) and is an update to the degree-20 model S20RTS (Ritsema *et al.* 1999). SAW642ANb (Panning *et al.* 2010) is a whole-mantle anisotropic model and is an update to SAW642AN (Panning & Romanowicz 2006) using new crustal corrections.

or S362ANI+M. We infer that S362WMANI was overparametrized given the constraints provided by the data set used in the inversion, and that it contained spurious structure. This is in agreement with the conclusions of Kustowski *et al.* (2008) who selected, based on resolution tests, the upper-mantle anisotropic model S362ANI rather than S362WMANI as their preferred model.

The question remains whether the mode-splitting data provide sufficient constraints on anisotropic structure to give credence to the anisotropy described by S362ANI+M or S362WMANI+M. We perform a synthetic test, similar to the one done by Kustowski *et al.* (2008) but now including mode-splitting data, to investigate whether the anisotropic variations in S362WMANI+M could be obtained through a velocity-anisotropy trade-off and therefore be spurious. For illustrative purposes, we multiply the isotropic spline coefficients $c_{ij\,\mathrm{S362WMANI+M}}^{\mathrm{ISO}}$ by an arbitrarily chosen and exaggerated factor of 3. The synthetic data $d^{\mathrm{SYN}}$ are obtained from $d^{\mathrm{SYN}} = A(3 \times c_{ij\,\mathrm{S362WMANI+M}}^{\mathrm{ISO}})$, where $A$ is the data-kernel matrix. The synthetic data are inverted for a whole-mantle anisotropic output model in the same way as we inverted the real data for S362WMANI+M. The anisotropic structure in the output model is then an artefact and represents the leakage of the isotropic signal into the anisotropic part of the model.

Fig. 16 shows the results of this resolution test at a depth of 2800 km in the lowermost mantle. The spurious anisotropic structure obtained by Kustowski *et al.* (2008) had a strong degree-2 component (Fig. 16f), similar to the isotropic variations at this depth (Fig. 16a). Such trade-offs in degree-2 and other even degrees are diminished with the use of modes in our inversions (Fig. 16e). Trade-offs persist in the odd degrees as the self-coupling splitting observations cannot constrain odd-degree structure. Similar comparisons in the uppermost mantle (150 km) and the transition zone (600 km) show that spurious anisotropic variations are negligible compared to the variations in S362WMANI+M. We infer from this experiment that the inclusion of mode-splitting data reduces the

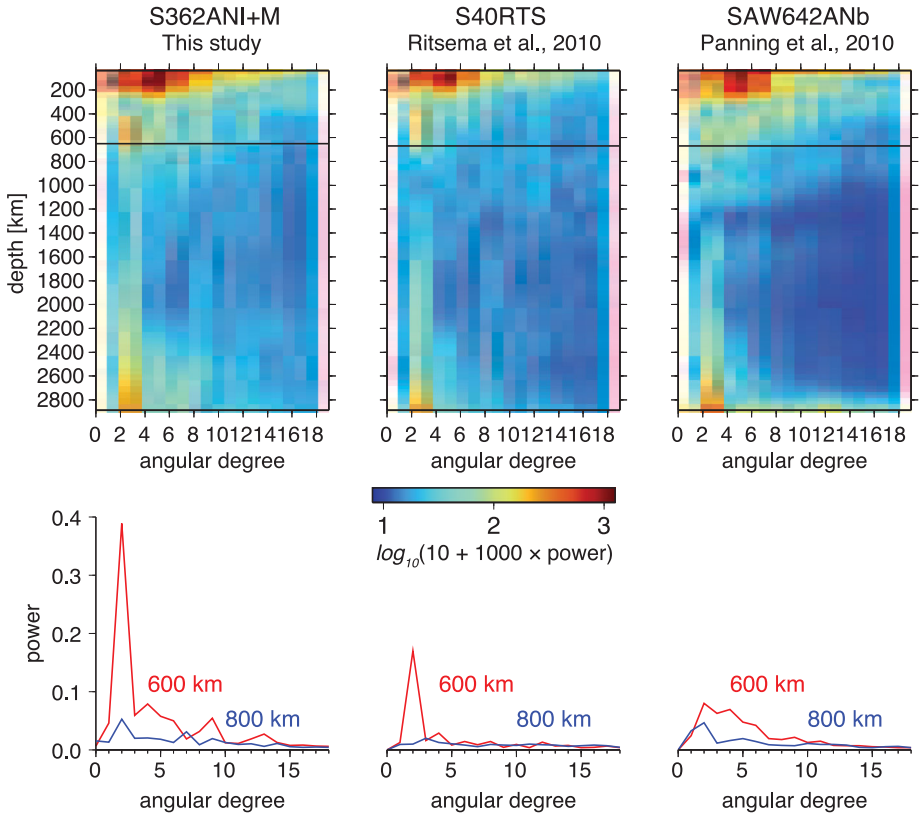


**Figure 12.** Power spectrum of shear wave velocity heterogeneity in the recent models S362ANI+M (this study), S40RTS (Ritsema *et al.* 2010) and SAW642ANb (Panning *et al.* 2010), plotted using a logarithmic colour scale. The black line in the upper panels denotes the 650-km boundary. Bottom panel shows power on a linear scale.

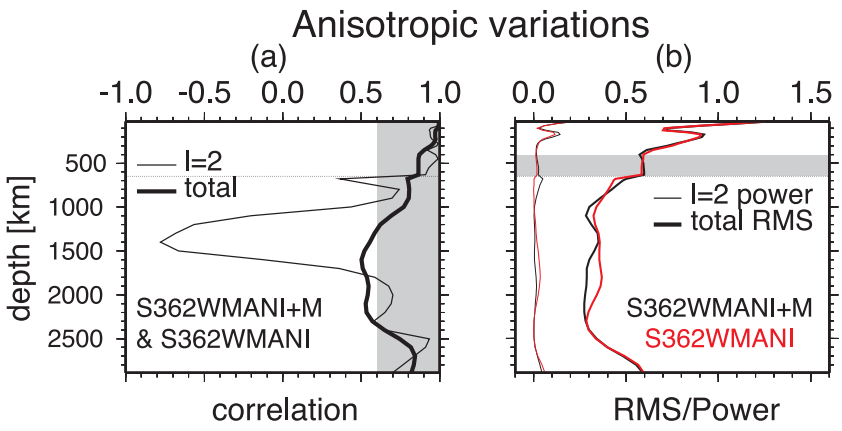


**Figure 13.** Comparisons between the anisotropic parts ($\delta a_S$) of whole-mantle anisotropic model S362WMANI+M and the earlier model S362WMANI. (a) The correlations between the anisotropic variations of the two models at degree-2 and for all degrees. (b) The power of degree-2 variations and the total rms values of radial anisotropy in the two models.

trade-offs between isotropic and anisotropic structure at the low and even degrees, especially in the lowermost mantle.

The normal-mode splitting functions included in our modelling provide constraints only on the even-degree structure. Becker & Boschi (2002) noted a consistently higher spectral power for isotropic velocities at even rather than at odd degrees up to degree 12 in S20RTS and suggested that splitting functions could be the cause of this pattern. The even-degree pattern is also observed in the recent model S40RTS but not in the isotropic parts of the models S362ANI+M and SAW642ANb (Fig. 17), both of which include long-period waveforms. It is unclear whether this 'zebra' pattern is indeed a real feature of the Earth's mantle at depths of ~300–650 km or is caused by the modelling approach and the resolving power of data. We solve for an upper-mantle anisotropic model without including the waveforms and by employing the same weighting of other data sets and regularization as used in constructing S362ANI+M. The power spectrum of the resulting model shows that the power of the lowest odd-degree structure (degrees 1 and 3) is diminished in the absence of long-period waveforms. Reduced power is also seen in the higher odd degrees but is not as systematic as seen in S40RTS; other choices such as norm damping versus smoothness damping could perhaps explain the differences at higher degrees. We infer that the use of long-period waveforms in S362ANI+M provides odd-degree sensitivity at the longest wavelengths not afforded by self-coupled splitting functions.

## 5 DISCUSSION

Overall, our results indicate that mode-splitting data can be fit consistently with other data sets while providing complementary constraints on Earth's structure. Even with the differences associated with the inclusion of modes, both S362ANI+M and S362ANI provide similar fits to the other types of data. The isotropic parts of S362ANI and S362ANI+M are highly correlated (~0.8 or more) at most depths and the changes due to the inclusion of modes are rather subtle. Most of the changes are in the amplitudes rather than in the patterns of heterogeneity. Although not described here, our experiments with the weighting of the mode-splitting data sets reveal that they indeed trade off with some of the body wave traveltime data sets. This trade-off is strongest for the *SKKS-SKS* data set where the variance reduction reduces from 47.5 per cent with S362WMANI (Fig. 15) to 42.7 per cent with S362WMANI+M (Fig. 5) when constraints from mode-splitting data are included.

The mode-splitting data require stronger heterogeneity in the transition zone, especially for the degree-2 variations (Fig. 18a). The most distinct features of the transition zone in S362ANI+M are the ~2–3 per cent faster-than-average velocities beneath major subduction zones. In particular, the faster-than-average anomalies associated with the South American subduction zone are more laterally extensive in S362ANI+M than in S362ANI and are similar to other isotropic shear velocity models that incorporate normal-mode splitting functions (e.g. Ritsema *et al.* 2010). These features extend horizontally for several hundreds of kilometres without continuing to the lower mantle and have been interpreted as flattening of slabs (Fukao *et al.* 2001) or their accumulation in the transition zone. Such accumulation of slab material could potentially be explained by chemical buoyancy of the subducted material (Ringwood & Irifune 1988), by folding due to viscosity contrasts (Gurnis & Hager 1988), or resistance due to the endothermic phase change across the boundary (Tackley *et al.* 1993).

The change in isotropic heterogeneity across the 650-km discontinuity, marked by a distinct decrease in amplitude, is more abrupt in S362ANI+M than in earlier models with similar vertical parametrizations (e.g. Gu *et al.* 2001; Kustowski *et al.* 2008, Figs 18a and b). We solve for but do not plot the lateral variations of the 410-km discontinuity as it is very similar to Kustowski *et al.* (2008). The *SS*-precursor data used in our inversions are the same as in Kustowski *et al.* (2008), while the mode-splitting data have limited sensitivity to topographies of transition-zone discontinuities. Therefore, S362ANI+M shows depressions in the 650-km discontinuity beneath the slab-like anomalies that are in broad agreement with other studies (Shearer & Masters 1992; Flanagan & Shearer 1998; Gu & Dziewoński 2002; Houser *et al.* 2008a; Kustowski *et al.* 2008). However, the trade-off between velocity and topography of transition-zone discontinuities (e.g. Gu *et al.* 2003) results in slightly perturbed discontinuities to compensate for the strong velocity heterogeneity in the transition zone (Fig. 18a). For example, the 650-km discontinuity beneath South America is further depressed by ~3 km in S362ANI+M as compared with S362ANI.

Lateral variations in radial anisotropy are imaged in the boundary regions of the Earth's mantle with varying degrees of robustness. The strongest anisotropic anomalies observed globally in the uppermost mantle are largely devoid of trade-offs with isotropic

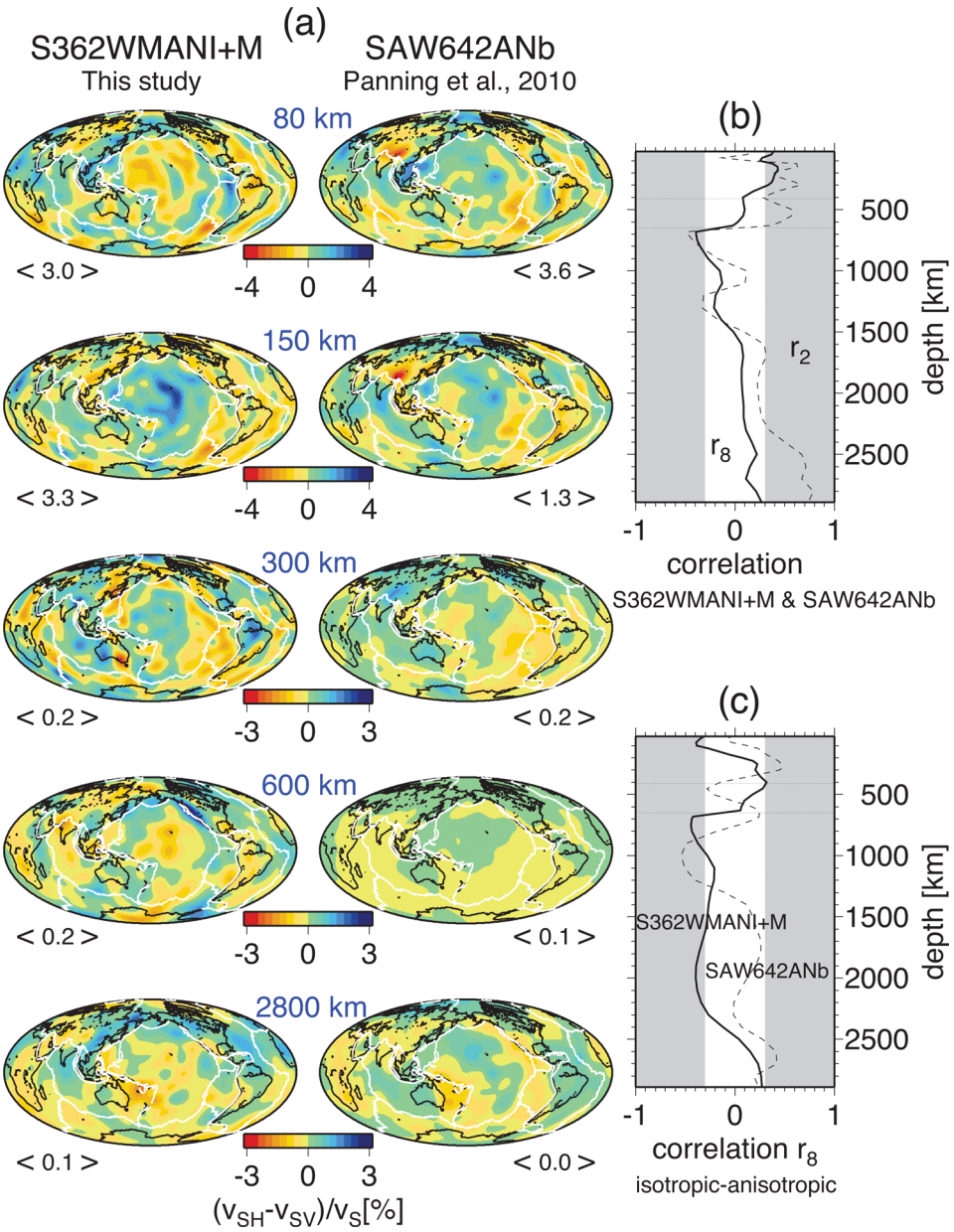


**Figure 14.** (a) Anisotropic velocity variations $(v_{SH} - v_{SV})/v_S$ in S362WMANI+M and SAW642ANb. Average anisotropy at each depth, as specified in $< >$, has been removed to eliminate the contribution from the reference models that are different in the two models. (b) Correlation between S362WMANI+M and SAW642ANb calculated up to spherical harmonic degrees 2 (dashed line) and 8 (solid line). (c) Correlation between isotropic and anisotropic variations in S362WMANI+M (solid line) and SAW642ANb (dashed line) calculated up to spherical harmonic degree 8. The dotted lines in (b) and (c) indicate the 410- and 650-km discontinuities and the shaded areas indicate correlations lower than –0.3 and higher than 0.3.

structure. The *a*-axis of dry olivine aligns parallel to flow direction, resulting in $v_{SH} > v_{SV}$ for regions with horizontal flow and $v_{SV} > v_{SH}$ for regions with vertical flow (e.g. Nicolas & Christensen 1987; Mainprice *et al.* 2000). The features in the shallowest mantle with $v_{SH} > v_{SV}$ should therefore suggest a dominant alignment of anisotropic crystals arising from horizontal flow in this ductile region of the mantle (Becker *et al.* 2008). However, this simple interpretation is hindered by factors like activation of other slip systems in wet olivine under high-stress conditions (e.g. Jung & Karato 2001; Karato *et al.* 2008; Ohuchi & Irifune 2013), influence of melt distribution on olivine LPO (Holtzman *et al.* 2003; Holtzman & Kendall 2010) or other potential mechanisms (e.g. Faccenda *et al.* 2008; Greve & Savage 2009).

The rms amplitude of anisotropic heterogeneity is smallest in the mid-mantle (1000–2400 km), and the mode-splitting data favour an even lower rms anisotropy with S362WMANI+M than was imaged in S362WMANI. The absence of large-scale anisotropy in the mid-mantle could be explained by diffusion creep (Karato 1998), which would inhibit alignment of minerals in preferred orientations (Karato 1988). The limited anisotropy detected in the mid-mantle is also consistent with the largely isotropic behaviour of its constituent minerals, perovskite and ferropericlase, at the relevant temperatures and pressures (e.g. Wentzcovitch *et al.* 2004; Li *et al.* 2006; Marquardt *et al.* 2009).

In the transition zone, there is hardly any agreement ($R_8 \sim 0.0$) on the anisotropic variations between our whole-mantle anisotropic

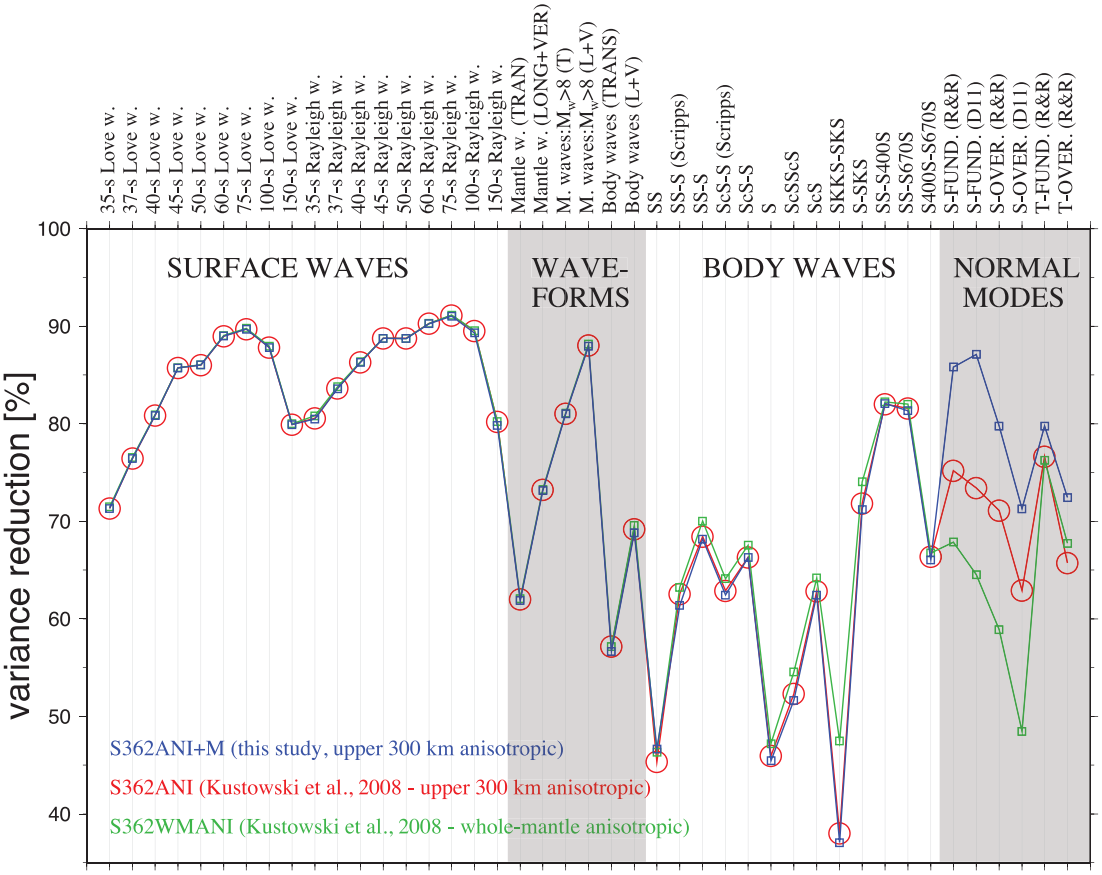


**Figure 15.** Different data sets and corresponding variance reductions achieved by S362ANI+M (this study) and the models S362ANI and S362WMANI from Kustowski *et al.* (2008). The labels are the same as that of Fig. 5.

model S362WMANI+M and that of Panning *et al.* (2010). While Panning *et al.* (2010) observed large-scale $v_{SV} > v_{SH}$ anomalies in the transition zone around the Pacific and associated them with subducting slabs, S362WMANI+M exhibits a variety of features at such depths. A $v_{SV} > v_{SH}$ anomaly is observed beneath South America which could be related to the subducting plate whose isotropic signature is imaged down to ∼1000 km. Other anisotropic anomalies with $v_{SH} > v_{SV}$ are observed in the transition zone beneath North America and the Northwest Pacific. Only wadsleyite, the olivine-polymorph at 410–520 km, is known to be anisotropic, while its higher-pressure polymorph (ringwoodite) and majorite garnet are nearly isotropic at transition-zone conditions (e.g. Zha *et al.* 1997; Mainprice *et al.* 2000). Therefore, the localized anisotropy observed in S362WMANI+M at the bottom of the transition zone would require a different mechanism. One mechanism could be the SPO of laminated garnetite sourced from the oceanic crust of subducting plates (Karato 1997).

In the lowermost mantle, several circum-Pacific $v_{SH} > v_{SV}$ variations in S362WMANI+M beneath Western Pacific, Alaska and the Caribbean are broadly consistent with regional studies (e.g Lay & Young 1991; Kendall & Silver 1996; Matzel *et al.* 1996). The small-scale features beneath the Central Pacific show mixed fast $v_{SV}$ or $v_{SH}$, roughly in agreement with regional studies of shear wave splitting data (e.g Vinnik *et al.* 1995, 1998; Pulliam & Sen 1998). The large-scale $v_{SV} > v_{SH}$ features may imply vertical flow in the superplumes (Panning & Romanowicz 2004), while the circum-Pacific $v_{SH} > v_{SV}$ features may imply horizontal flow in regions where subducting slabs reach the CMB. However, such a straightforward interpretation does not explain the strongest $v_{SV} > v_{SH}$ anomalies in both S362WMANI+M and SAW642ANb observed beneath the Tonga-Kermadec and New Hebrides trenches, which are at the edge of rather than being co-located with the Pacific superplume. Furthermore, the experimental results disagree on the slip systems of post-perovskite (e.g. Merkel *et al.* 2007; Mao *et al.* 2010; Miyagi *et al.* 2010) as well as the role of partial melt (e.g. Kendall & Silver 1996; Hirose *et al.* 1999), ferropericlase and perovskite (e.g. Yamazaki & Karato 2002; Mainprice *et al.* 2008), factors which influence greatly the interpretation of detected anisotropy in terms of flow in the lowermost mantle.

The parameter space explored in the current study is limited; we do not explicitly consider variations in density and impose a constant relationship between variations in compressional and shear wave velocities. The gravest normal modes, in particular, have additional sensitivity to density variations in the mantle due to the effects of self-gravitation (e.g. Dahlen & Tromp 1998). Departures from constant scaling factors have been suggested for the compressional velocities (e.g. Su & Dziewoński 1997; Masters *et al.* 2000a) and density (e.g. Ishii & Tromp 1999) in the deep mantle. However, several studies have shown the limited resolution provided by mode-splitting data to density structure (e.g. Resovsky & Ritzwoller 1999a; Romanowicz 2001; Kuo & Romanowicz 2002). We performed additional inversions where density was scaled to isotropic shear velocity with a constant scaling factor of 0.33. The correlations for both isotropic and anisotropic variations between S362WMANI+M and the resulting model were uniformly high ($R > 0.95$). This suggests that the patterns of anisotropic shear

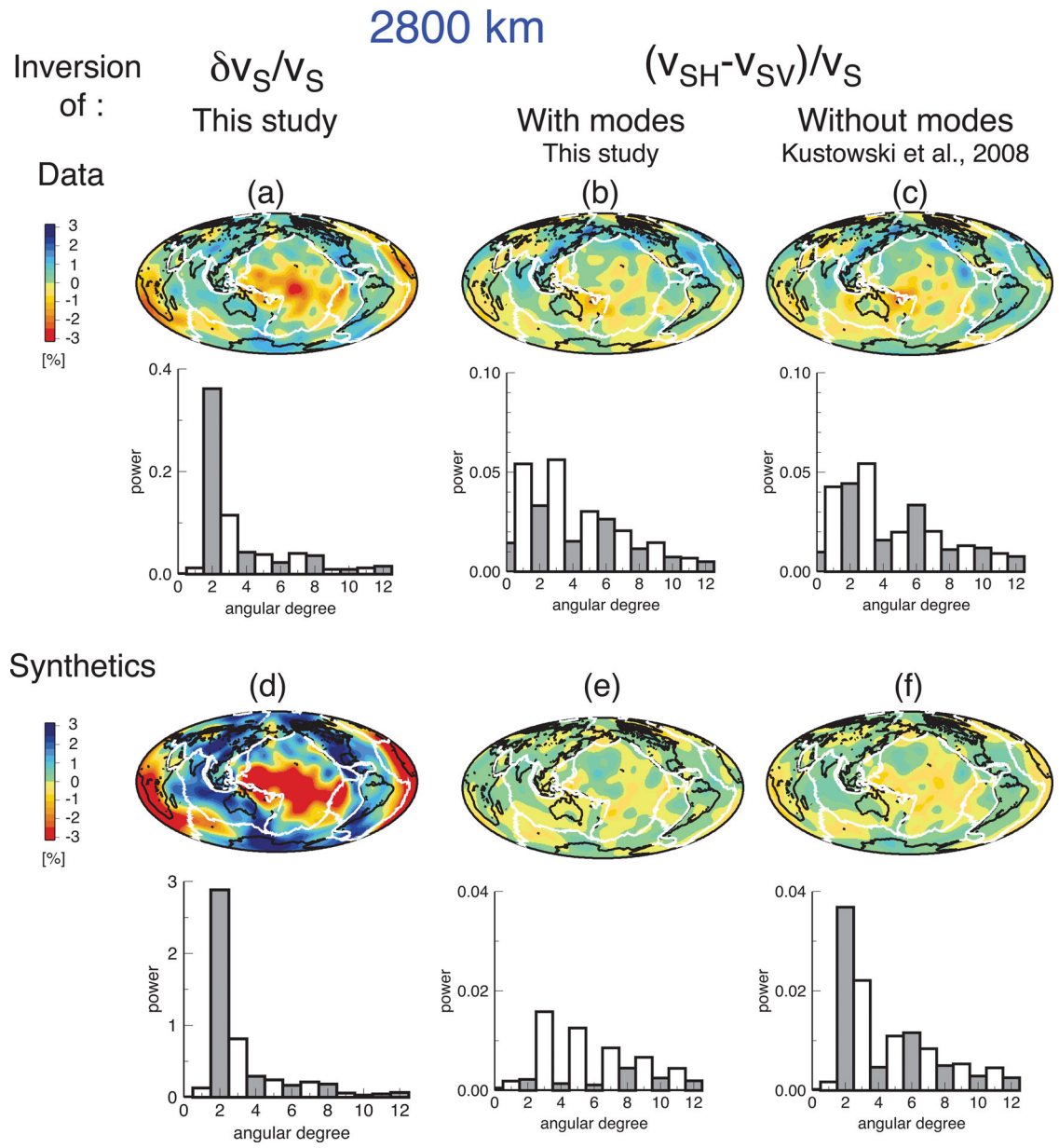


**Figure 16.** Synthetic resolution test: (a, b) Isotropic and anisotropic variations in the whole-mantle anisotropic model S362WMANI+M at a depth of 2800 km. (c) Anisotropic variations from S362WMANI obtained without mode-splitting data. (d, e) Isotropic and anisotropic variations obtained by inverting the synthetic data predicted by the isotropic $3(\delta v_S/v_S)_{\mathrm{S362WMANI+M}}$ input model at a depth of 2800 km. (f) Anisotropic variations obtained by inverting all synthetic data except mode-splitting coefficients. Global averages have been removed before plotting. The spectra of the lateral variations in each figure are plotted as a bar graph, with even degrees in grey and odd degrees in white.

velocity are not much influenced by whether or not density variations are accounted for in the inversions. A detailed analysis of the scaling ratios and their resolution with current data sets will be the subject of future work.

Limitations of the theoretical approximations used in our modelling is another aspect that is not explored in this study. We include long-period waveforms in the context of the path-average approximation (e.g. Woodhouse & Dziewoński 1984). Modern numerical techniques, such as the spectral element method (e.g. Komatitsch *et al.* 2002), can theoretically attribute every portion of the seismogram to heterogeneity using adjoint methods (e.g. Tarantola 1984; Tromp *et al.* 2005; Liu & Tromp 2006, 2008). Adjoint techniques in tomography have been implemented at local (Tape *et al.* 2009) and regional scales (Fichtner *et al.* 2009; Zhu *et al.* 2012), while computational costs have impeded their application at global scales (e.g. Lekić & Romanowicz 2011). Recent theoretical approaches also take into account volumetric sensitivity for body waves (Dahlen *et al.* 2000; Zhao *et al.* 2000) and surface waves (Li & Romanowicz 1995; Marquering *et al.* 1996; Yoshizawa & Kennett 2002b; Peter *et al.* 2007; Lin *et al.* 2010). Several authors have used such frequency-dependent sensitivity of body wave traveltimes in tomographic inversions (e.g. Montelli *et al.* 2004a,b; Sigloch *et al.* 2008; Tian *et al.* 2011). Recent tomographic studies using body and surface waves have shown that similar structures can be obtained using either theory depending on the choices of parametrization and regularization (Spetzler *et al.* 2002; Sieminski *et al.* 2004; Boschi

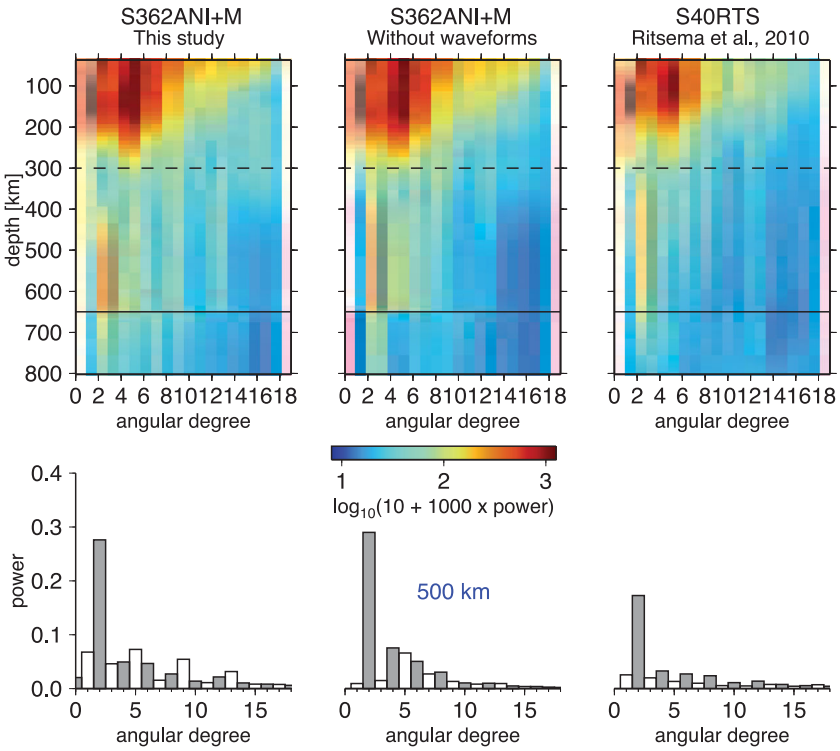


**Figure 17.** (Top panels) The power spectrum of isotropic shear velocities in the mantle down to 800 km for S362ANI+M, a version of S362ANI+M inverted without waveform data, and S40RTS (Ritsema *et al.* 2010). The power spectrum is plotted with a logarithmic scale. (Bottom panels) The variations in power at a depth of 500 km are shown as a bar graph, with even degrees in grey and odd degrees in white.

*et al.* 2006; Trampert & Spetzler 2006) and that data coverage may be more important than a sophisticated theory (van der Hilst & de Hoop 2005). A more accurate theory is clearly needed for recovering small-scale heterogeneity (e.g. Tromp *et al.* 2005; Chen *et al.* 2007; Peter & Boschi 2009); we focus on modelling different types of data to get complementary constraints for large-scale mantle structure.

## 6 CONCLUSIONS

In this study, (i) we develop a new method to invert jointly four distinct types of seismic data for anisotropic shear velocities and discontinuity topographies in the Earth's mantle while accounting accurately for the crustal structure. (ii) We show that the mode-splitting data require strong isotropic $v_S$ heterogeneity in the transition zone and changes to the Southern Hemisphere in the mid- to lower mantle. (iii) We report the improved consistency between recent studies on the long-wavelength isotropic structure, especially in the transition zone and the lower mantle. (iv) We show that the data sets used in this study, especially the mode-splitting data, do not require radial anisotropy in the deep mantle. (v) We demonstrate that the mode-splitting data suppress spurious anisotropic anomalies in the mid-mantle and reduce even-degree trade-offs between anisotropic and isotropic variations in the lowermost mantle.

The main outcome of this study is the upper-mantle anisotropic model S362ANI+M and its isotropic and whole-mantle anisotropic versions, S362ISO+M and S362WMANI+M. Selecting the more robust representation of Earth structure requires an integrated analysis of the data fits, resolution tests and comparisons with other studies. Fits to the surface wave data are clearly improved by including anisotropy in the uppermost ~300 km of the mantle; this result disfavours purely isotropic variations in the mantle as described by S362ISO+M. Some anisotropic features in S362WMANI+M below ~300 km are broadly consistent with petrological constraints and regional shear wave-splitting studies. The reductions in spurious anisotropy with the addition of mode-splitting data also lend some credence to these features. However, there is limited agreement between various studies on anisotropic variations in the mantle. Also, the bulk of the data sets used in this study does not show appreciable improvements in fit with the addition of anisotropy in the deep mantle. We therefore select S362ANI+M as our preferred model in this study.

Our modelling approach can be readily extended to retrieve multiresolution models whose long-wavelength components are compatible with mode-splitting data. Future work on resolving anisotropic shear velocity will benefit from the further development and consideration of toroidal-mode-splitting functions as well as very-long-period surface wave phase anomalies. Additional constraints on anisotropy in the lowermost mantle will also come from expanded data sets of traveltime measurements of phases such as *SKS* and *SKKS*. With the recent surge in the amounts of different data (e.g. Ekström 2011; Deuss *et al.* 2013), constraining anisotropic shear velocity in hitherto undersampled regions of the Earth's mantle may become an attainable goal in the future.

## ACKNOWLEDGEMENTS

This material is based on work supported by National Science Foundation Grants EAR-08-38093 and EAR-13-15984. We thank Arwen Deuss, Joe Resovsky, Michael Ritzwoller and Jeroen Tromp for making their catalogues of splitting functions available, Guy Masters for making the traveltimes measured at Scripps available and Mark Panning and Jeroen Ritsema for posting their models online

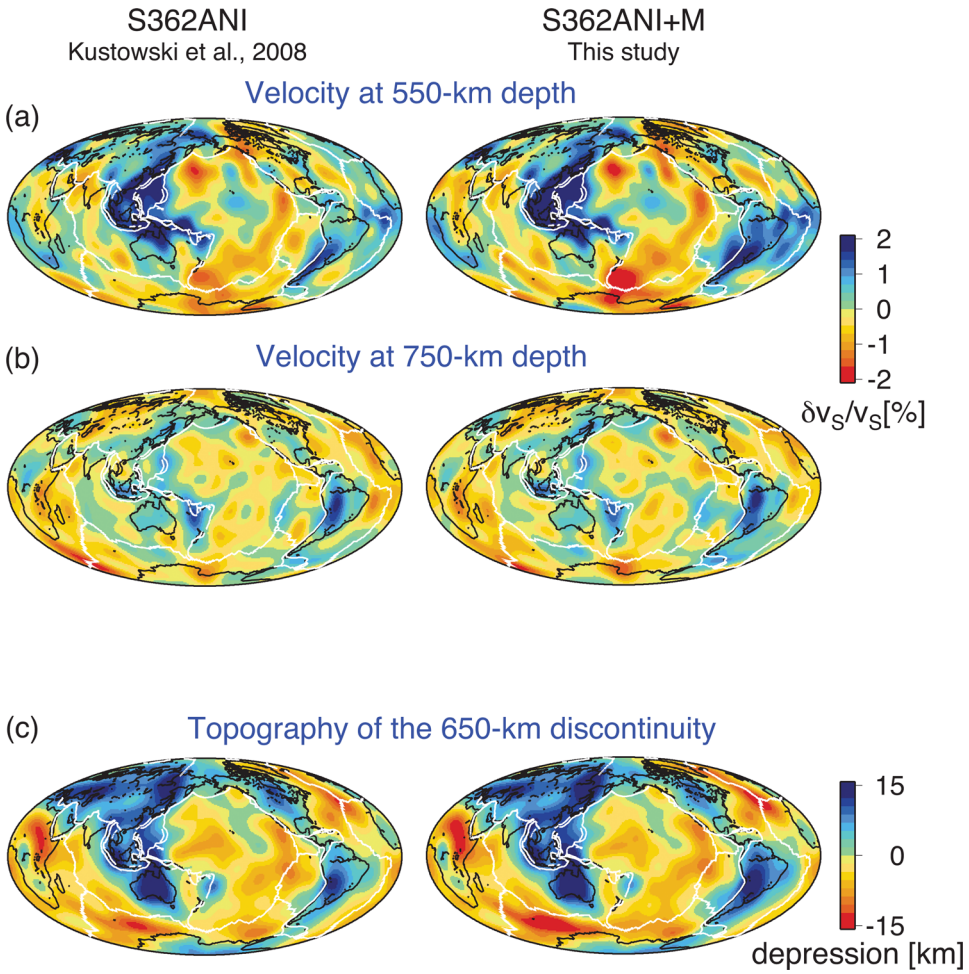


**Figure 18.** Isotropic shear wave velocity variations above (a) and below the 650-km discontinuity (b) and topography of the 650-km discontinuity (c) in S362ANI and our preferred model S362ANI+M.

in the electronic format. We benefited from discussions with Adam Dziewoński and Bogdan Kustowski. Some of the figures were made with GMT (http://gmt.soest.hawaii.edu). The models are available online at http://www.ldeo.columbia.edu/~moulik.

## REFERENCES

Anderson, D.L. & Dziewoński, A.M., 1982. Upper mantle anisotropy: evidence from free oscillations, *Geophys. J. Int.,* **69**(2), 383–404.

Bassin, C., Laske, G. & Masters, G., 2000. The current limits of resolution for surface wave tomography in North America, *EOS, Trans. Am. geophys. Un.,* **81,** F897.

Becker, T.W. & Boschi, L., 2002. A comparison of tomographic and geodynamic mantle models, *Geochem. Geophys. Geosyst.,* **3,** doi:10.1029/2001GC000168.

Becker, T.W., Kellogg, J.B., Ekström, G. & O'Connell, R.J., 2003. Comparison of azimuthal seismic anisotropy from surface waves and finite strain from global mantle-circulation models, *Geophys. J Int.,* **155,** 696–714.

Becker, T.W., Kustowski, B. & Ekström, G., 2008. Radial seismic anisotropy as a constraint for upper mantle rheology, *Earth planet. Sci. Lett.,* **267,** 213–227.

Beghein, C. & Trampert, J., 2004. Probability density functions for radial anisotropy: implications for the upper 1200 km of the mantle, *Earth planet. Sci. Lett.,* **217,** 151–162.

Beghein, C., Resovsky, J.S. & Trampert, J., 2002. P and S tomography using normal-mode and surface waves data with a neighbourhood algorithm, *Geophys. J. Int.,* **149,** 646–658.

Beghein, C., Resovsky, J. & van der Hilst, R.D., 2008. The signal of mantle anisotropy in the coupling of normal modes, *Geophys. J. Int.,* **175,** 1209–1234.

Bercovici, D. & Karato, S., 2003. Whole-mantle convection and the transition-zone water filter, *Nature,* **425,** 39–44.

Bolton, H. & Masters, G., 2001. Travel times of P and S from the global digital seismic networks: implications for the relative variation of P and S velocity in the mantle, *J. geophys. Res.,* **106,** 13 527–13 540.

Boschi, L. & Dziewoński, A.M., 1999. High- and low-resolution images of the Earth's mantle: implications of different approaches to tomographic modeling, *J. geophys. Res.,* **104**(B11), 25 567–25 594.

Boschi, L., Becker, T.W., Soldati, G. & Dziewoński, A.M., 2006. On the relevance of Born theory in global seismic tomography, *Geophys. Res. Lett.,* **33,** L06302, doi:10.1029/2005GL025063.

Burgos, G., Montagner, J., Beucler, E., Capdeville, Y., Mocquet, A. & Drilleau, M., 2014. Oceanic lithosphere-asthenosphere boundary from surface wave dispersion data, *J. geophys. Res.,* **119,** 1079–1093.

Chang, S.J., Ferreira, A., Ritsema, J. & van Heijst, H.J., 2014. Global radially anisotropic mantle structure from multiple datasets: a review, current challenges, and outlook, *Tectonophysics,* **617,** doi:10.1016/j.tecto.2014.01.033.

Chen, P., Jordan, T.H. & Zhao, L., 2007. Full three-dimensional tomography: a comparison between the scattering-integral and adjoint-wavefield methods, *Geophys. J. Int.,* **170**(1), 175–181.

Chen, W.-P. & Brudzinski, M.R., 2003. Seismic anisotropy in the mantle transition zone beneath Fiji-Tonga, *Geophys. Res. Lett.,* **30**(13), 1682, doi:10.1029/2002GL016330.

Dahlen, F.A. & Tromp, J., 1998. *Theoretical Global Seismology,* Princeton Univ. Press.

Dahlen, F.A., Hung, S.H. & Nolet, G., 2000. Fréchet kernels for finite-frequency traveltimes—I. Theory, *Geophys. J. Int.,* **141,** 157–174.

Debayle, E. & Ricard, Y., 2012. A global shear velocity model of the upper mantle from fundamental and higher Rayleigh mode measurements, *J. geophys. Res.,* **117,** B10308, doi:10.1029/2012JB009288.

Deuss, A., Ritsema, J. & van Heijst, H., 2011. Splitting function measurements for Earth's longest period normal modes using recent large earthquakes, *Geophys. Res. Lett.,* **38**(4), L04303, doi:10.1029/2010GL046115.

Deuss, A., Ritsema, J. & van Heijst, H., 2013. A new catalogue of normal-mode splitting function measurements up to 10 mHz, *Geophys. J. Int.,* **193**(2), 920–937.

Durek, J.J. & Romanowicz, B., 1999. Inner core anisotropy inferred by direct inversion of normal mode spectra, *Geophys. J. Int.,* **139**(3), 599–622.

Dziewoński, A. & Woodward, R., 1992. Acoustic imaging at the planetary scale, in *Acoustical Imaging,* Vol. 19, pp. 785–797, eds Emert, H. & Harjes, H.-P., Plenum Press.

Dziewoński, A.M. & Anderson, D.L., 1981. Preliminary reference earth model, *Phys. Earth planet. Inter.,* **25**(4), 297–356.

Dziewoński, A.M. & Gilbert, F., 1976. The effect of small, aspherical perturbations on travel times and a re-examination of the corrections for ellipticity, *Geophys. J. Int.,* **44**(1), 7–17.

Dziewoński, A.M. & Woodhouse, J.H., 1983. An experiment in systematic study of global seismicity: centroid-moment tensor solutions for 201 moderate and large earthquakes of 1981, *J. geophys. Res.,* **88**(B4), 3247–3271.

Dziewoński, A.M., Chou, T.A. & Woodhouse, J.H., 1981. Determination of earthquake source parameters from waveform data for studies of global and regional seismicity, *J. geophys. Res.,* **86**(B4), 2825–2852.

Ekström, G., 2011. A global model of Love and Rayleigh surface wave dispersion and anisotropy, 25–250 s, *Geophys. J. Int.,* **187,** 1668–1686.

Ekström, G. & Dziewoński, A.M., 1998. The unique anisotropy of the Pacific upper mantle, *Nature,* **394,** 168–172.

Ekström, G., Tromp, J. & Larson, E., 1997. Measurements and global models of surface wave propagation, *J. geophys. Res.,* **102,** 8137–8157.

Faccenda, M., Burlini, L., Gerya, T.V. & Mainprice, D., 2008. Fault-induced seismic anisotropy by hydration in subducting oceanic plates, *Nature,* **455,** 1097–1100.

Ferreira, A.M.G., Woodhouse, J.H., Visser, K. & Trampert, J., 2010. On the robustness of global radially anisotropic surface wave tomography, *J. geophys. Res.,* **115,** B04313, doi:10.1029/2009JB006716.

Fichtner, A., Kennett, B.L.N., Igel, H. & Bunge, H.P., 2009. Full seismic waveform tomography for upper-mantle structure in the Australasian region using adjoint methods, *Geophys. J. Int.,* **179**(3), 1703–1725.

Flanagan, M.P. & Shearer, P.M., 1998. Global mapping of topography on transition zone velocity discontinuities by stacking SS precursors, *J. geophys. Res.,* **103**(B2), 2673–2692.

Foley, B.J. & Long, M.D., 2011. Upper and mid-mantle anisotropy beneath the Tonga slab, *Geophys. Res. Lett.,* **38,** L02303, doi:10.1029/2010GL046021.

Fouch, M.J. & Fischer, K.M., 1996. Mantle anisotropy beneath northwest Pacific subduction zones, *J. geophys. Res.,* **101,** 15 987–16 002.

French, S., Lekic, V. & Romanowicz, B., 2013. Waveform tomography reveals channeled flow at the base of the oceanic asthenosphere, *Science,* **342**(6155), 227–230.

Fukao, Y., Obayashi, M., Inoue, H. & Nenbai, M., 1992. Subducting slabs stagnant in the mantle transition zone, *J. geophys. Res.,* **97**(B4), 4809–4822.

Fukao, Y., Widiyantoro, S. & Obayashi, M., 2001. Stagnant slabs in the upper and lower mantle transition region, *Rev. Geophys.,* **39**(3), 291–323.

Gaboret, C., Forte, A.M. & Montagner, J., 2003. The unique dynamics of the Pacific Hemisphere mantle and its signature on seismic anisotropy, *Earth planet. Sci. Lett.,* **208**(3), 219–233.

Giardini, D., Li, X.-D. & Woodhouse, J.H., 1987. Three-dimensional structure of the Earth from splitting in free-oscillation spectra, *Nature,* **325,** 405–411.

Giardini, D., Li, X.-D. & Woodhouse, J.H., 1988. Splitting functions of long-period normal modes of the Earth, *J. geophys. Res.,* **93**(B11), 13 716–13 742.

Goes, S., Capitanio, F.A. & Morra, G., 2008. Evidence of lower-mantle slab penetration phases in plate motions, *Nature,* **451,** 981–984.

Grand, S.P., van der Hilst, R.D. & Widiyantoro, S., 1997. High resolution global tomography: a snapshot of convection in the Earth, *Geol. Soc. Am. TODAY,* **7**(4), 1–7.

Greve, S.M. & Savage, M.K., 2009. Modelling seismic anisotropy variations across the Hikurangi subduction margin, New Zealand, *Earth planet. Sci. Lett.,* **285,** 16–26.

Gu, Y.J. & Dziewoński, A.M., 2002. Global variability of transition zone thickness, *J. geophys. Res.: Solid Earth,* **107**(B7), 2135, doi:10.1029/2001JB000489.

Gu, Y.J., Dziewoński, A.M., Su, W. & Ekström, G., 2001. Models of the mantle shear velocity and discontinuities in the pattern of lateral heterogeneities, *J. geophys. Res.,* **106**(B6), 11 169–11 199.

Gu, Y.J., Dziewoński, A.M. & Ekström, G., 2003. Simultaneous inversion for mantle shear velocity and topography of transition zone discontinuities, *Geophys. J. Int.,* **154,** 559–583.

Gung, Y., Panning, M. & Romanowicz, B., 2003. Global anisotropy and the thickness of continents, *Nature,* **422**(6933), 707–711.

Gurnis, M. & Hager, B.H., 1988. Controls of the structure of subducted slabs, *Nature,* **335,** 317–321.

He, X. & Tromp, J., 1996. Normal-mode constraints on the structure of the Earth, *J. geophys. Res.,* **101**(B9), 20 053–20 082.

Hirose, K., Fei, Y., Ma, Y. & Mao, H.-k., 1999. The fate of subducted basaltic crust in the Earth's lower mantle, *Nature,* **397,** 53–56.

Holtzman, B.K. & Kendall, J.M., 2010. Organized melt, seismic anisotropy, and plate boundary lubrication, *Geochem. Geophys. Geosyst.,* **11,** Q0AB06, doi:10.1029/2010GC003296.

Holtzman, B.K., Kohlstedt, D.L. & Zimmerman, M.E., 2003. Melt segregation and strain partitioning: implications for seismic anisotropy and mantle flow, *Science,* **301,** 1227–1230.

Houser, C., Masters, G., Flanagan, M. & Shearer, P., 2008a. Determination and analysis of long-wavelength transition zone structure using SS precursors, *Geophys. J. Int.,* **174**(1), 178–194.

Houser, C., Masters, G., Shearer, P. & Laske, G., 2008b. Shear and compressional velocity models of the mantle from cluster analysis of long-period waveforms, *Geophys. J. Int.,* **174**(1), 195–212.

Ishii, M. & Tromp, J., 1999. Normal-mode and free-air gravity constraints on lateral variations in velocity and density of Earth's mantle, *Science,* **285,** 1231–1236.

Ishii, M. & Tromp, J., 2001. Even-degree lateral variations in the Earth's mantle constrained by free oscillations and the free-air gravity anomaly, *Geophys. J. Int.,* **145**(1), 77–96.

Jung, H. & Karato, S.-i., 2001. Water-induced fabric transitions in olivine, *Science,* **293,** 1460–1463.

Karato, S., 1988. The role of recrystallization in the preferred orientation of olivine, *Phys. Earth planet. Inter.,* **51,** 107–122.

Karato, S., 1997. On the separation of crustal component from subducted oceanic lithosphere near the 660 km discontinuity, *Phys. Earth planet. Inter.,* **99,** 103–111.

Karato, S., 1998. Seismic anisotropy in the deep mantle, boundary layers and the geometry of mantle convection, *Pure appl. Geophys.,* **151,** 565–587.

Karato, S.-i., 1992. On the Lehmann discontinuity, *Geophys. Res. Lett.,* **19**(22), 2255–2258.

Karato, S.-i., 1993. Importance of anelasticity in the interpretation of seismic tomography, *Geophys. Res. Lett.,* **20**(15), 1623–1626.

Karato, S.-i., Jung, H., Katayama, I. & Skemer, P., 2008. Geodynamic significance of seismic anisotropy of the upper mantle: new insights from laboratory studies, *Ann. Rev. Earth planet. Sci.,* **36**(1), 59–95.

Kendall, J.M. & Silver, P.G., 1996. Constraints from seismic anisotropy on the nature of the lowermost mantle, *Nature,* **381,** 409–412.

Komatitsch, D. & Tromp, J., 2002a. Spectral-element simulations of global seismic wave propagation—II. Three-dimensional models, oceans, rotation and self-gravitation, *Geophys. J. Int.,* **150**(1), 303–318.

Komatitsch, D. & Tromp, J., 2002b. Spectral-element simulations of global seismic wave propagation – I. Validation, *Geophys. J. Int.,* **149**(2), 390–412.

Komatitsch, D., Ritsema, J. & Tromp, J., 2002. The spectral-element method, Beowulf computing, and global seismology, *Science,* **298,** 1737–1742.

Kuo, C. & Romanowicz, B., 2002. On the resolution of density anomalies in the Earth's mantle using spectral fitting of normal-mode data, *Geophys. J. Int.,* **150**(1), 162–179.

Kustowski, B., 2007. Modeling the anisotropic shear-wave velocity structure in the Earth's mantle on global and regional scales, *PhD thesis,* Harvard Univ., Cambridge, Mass.

Kustowski, B., Ekström, G. & Dziewoński, A.M., 2007. Nonlinear crustal corrections for normal-mode seismograms, *Bull. seism. Soc. Am.,* **97**(5), 1756–1762.

Kustowski, B., Ekström, G. & Dziewoński, A.M., 2008. Anisotropic shear-wave velocity structure of the Earth's mantle: a global model, *J. geophys. Res.,* **113,** B06306, doi:10.1029/2007JB005169.

Lancaster, P. & Salkauskas, K., 1986. *Curve and Surface Fitting: An Introduction,* Academic Press.

Laske, G. & Masters, G., 1996. Constraints on global phase velocity maps from long-period polarization data, *J. geophys. Res.,* **101**(B7), 16 059–16 075.

Lay, T. & Young, C.J., 1991. Analysis of seismic SV waves in the core's penumbra, *Geophys. Res. Lett.,* **18**(8), 1373–1376.

Lay, T., Williams, Q., Garnero, E.J., Kellogg, L. & Wysession, M., 1998. Seismic wave anisotropy in the D″ region and its implications, *Core-Mantle Boundary Reg.,* **28,** 299–318.

Lekić, V. & Romanowicz, B., 2011. Inferring upper-mantle structure by full waveform tomography with the spectral element method, *Geophys. J. Int.,* **185**(2), 799–831.

Lekić, V., Panning, M. & Romanowicz, B., 2010. A simple method for improving crustal corrections in waveform tomography, *Geophys. J. Int.,* **182**(1), 265–278.

Li, L., Weidner, D.J., Brodholt, J. & Alfe, D., 2006. Elasticity of $CaSiO_3$ perovskite at high pressure and high temperature, *Phys. Earth planet. Inter.,* **155,** 249–259.

Li, X., Giardini, D. & Woodhouse, J., 1991. Large-scale three-dimensional even-degree structure of the Earth from splitting of long-period normal modes, *J. geophys. Res.,* **96**(B1), 551–577.

Li, X.-D. & Romanowicz, B., 1995. Comparison of global waveform inversions with and without considering cross-branch modal coupling, *Geophys. J. Int.,* **121**(3), 695–709.

Lin, F.C., Lin, F.-C., Ritzwoller, M. & Ritzwoller, M.H., 2010. Empirically determined finite frequency sensitivity kernels for surface waves, *Geophys. J. Int.,* **182**(2), 923–932.

Liu, Q. & Tromp, J., 2006. Finite-frequency kernels based on adjoint methods, *Bull. seism. Soc. Am.,* **96**(6), 2383–2397.

Liu, Q. & Tromp, J., 2008. Finite frequency sensitivity kernels for global seismic wave propagation based upon adjoint methods, *Geophys. J. Int.,* **174,** 265–286.

Liu, X. & Dziewoński, A., 1998. Global analysis of shear wave velocity anomalies in the lower-most mantle, in *The Core-Mantle Boundary Region, Geodyn. Ser.,* Vol. 28, pp. 21–36, eds Gurnis, M., Wysession, M., Knittle, E. & Buffett, B., American Geophysical Union.

Long, M.D., 2009. Complex anisotropy in D″ beneath the eastern Pacific from SKS–SKKS splitting discrepancies, *Earth planet. Sci. Lett.,* **283,** 181–189.

Long, M.D. & Becker, T.W., 2010. Mantle dynamics and seismic anisotropy, *Earth planet. Sci. Lett.,* **297**(3–4), 341–354.

Mainprice, D., Barruol, G. & Ben Ismail, W., 2000. The seismic anisotropy of the Earth's mantle: from single crystal to polycrystal, in *Earth's Deep Interior: Mineral Physics and Tomography from the Atlantic to the Global Scale, Geophys. Monogr. Ser.,* pp. 237–264, eds Karato, S.-I., Forte, A., Liebermann, R., Masters, G. & Stixrude, L., American Geophysical Union.

Mainprice, D., Tommasi, A., Ferré, D., Carrez, P. & Cordier, P., 2008. Predicted glide systems and crystal preferred orientations of polycrystalline silicate Mg-Perovskite at high pressure: implications for the seismic anisotropy in the lower mantle, *Earth planet. Sci. Lett.,* **271,** 135–144.

Mao, W.L., Meng, Y. & Mao, H., 2010. Elastic anisotropy of ferromagnesian post-perovskite in Earth's D″ layer, *Phys. Earth planet. Inter.,* **180,** 203–208.

Marone, F. & Romanowicz, B., 2007. The depth distribution of azimuthal anisotropy in the continental upper mantle, *Nature,* **447,** 198–201.

Marquardt, H., Speziale, S., Reichmann, H.J. & Frost, D.J., 2009. Elastic shear anisotropy of ferropericlase in Earth's lower mantle, *Science,* **324,** 224–226.

Marquering, H., Snieder, R. & Nolet, G., 1996. Waveform inversions and the significance of surface-wave mode coupling, *Geophys. J. Int.,* **124**(1), 258–278.

Masters, G., Laske, G., Bolton, H. & Dziewoński, A., 2000a. The relative behavior of shear velocity, bulk sound speed, and compressional velocity in the mantle: implications for chemical and thermal structure, in *Earth's Deep Interior: Mineral Physics and Tomography from the Atlantic to the Global Scale, Geophys. Monogr. Ser.,* Vol. 117, pp. 63–87, eds Karato, S., Forte, A., Liebermann, R., Masters, G. & Stixrude, L., American Geophysical Union.

Masters, G., Laske, G. & Gilbert, F., 2000b. Autoregressive estimation of the splitting matrix of free-oscillation multiplets, *Geophys. J. Int.,* **141**(1), 25–42.

Masters, G., Laske, G. & Gilbert, F., 2000c. Matrix autoregressive analysis of free-oscillation coupling and splitting, *Geophys. J. Int.,* **143**(2), 478–489.

Matzel, E., Sen, M.K. & Grand, S.P., 1996. Evidence for anisotropy in the deep mantle beneath Alaska, *Geophys. Res. Lett.,* **23**(18), 2417–2420.

Meier, U., Curtis, A. & Trampert, J., 2007. Fully nonlinear inversion of fundamental mode surface waves for a global crustal model, *Geophys. Res. Lett.,* **34,** L16304, doi:10.1029/2007GL030989.

Menke, W., 1989. *Geophysical Data Analysis: Discrete Inverse Theory,* Academic Press.

Merkel, S., McNamara, A.K., Kubo, A., Speziale, S., Miyagi, L., Meng, Y., Duffy, T.S. & Wenk, H.-R., 2007. Deformation of $(Mg,Fe)SiO_3$ post-perovskite and D″ anisotropy, *Science,* **316,** 1729–1732.

Miyagi, L., Kanitpanyacharoen, W., Kaercher, P., Lee, K.K.M. & Wenk, H.-R., 2010. Slip systems in $MgSiO_3$ post-perovskite: implications for D″ anisotropy, *Science,* **329,** 1639–1641.

Mochizuki, E., 1986. The free oscillations of an anisotropic and heterogeneous Earth, *Geophys. J. Int.,* **86**(1), 167–176.

Montagner, J. & Anderson, D.L., 1989. Petrological constraints on seismic anisotropy, *Phys. Earth planet. Inter.,* **54,** 82–105.

Montelli, R., Nolet, G., Dahlen, F.A., Masters, G., Engdahl, E.R. & Hung, S.-H., 2004a. Finite-frequency tomography reveals a variety of plumes in the mantle, *Science,* **303,** 338–343.

Montelli, R., Nolet, G., Masters, G., Dahlen, F.A. & Hung, S.H., 2004b. Global P and PP traveltime tomography: rays versus waves, *Geophys. J. Int.,* **158**(2), 637–654.

Nettles, M. & Dziewoński, A.M., 2008. Radially anisotropic shear velocity structure of the upper mantle globally and beneath North America, *J. geophys. Res.,* **113**(B2), B02303, doi:10.1029/2006JB004819.

Nicolas, A. & Christensen, N., 1987. Formation of anisotropy in upper mantle peridotites: a review, in *Composition, Structure and Dynamics of the Lithosphere-Asthenosphere System, Geodyn. Ser.,* pp. 111–123, edsFuchs, K. & Froidevaux, C., American Geophysical Union.

Nowacki, A., Wookey, J. & Kendall, J.M., 2010. Deformation of the lowermost mantle from seismic anisotropy, *Nature,* **467,** 1091–1094.

Ohuchi, T. & Irifune, T., 2013. Development of A-type olivine fabric in water-rich deep upper mantle, *Earth planet. Sci. Lett.,* **362,** 20–30.

Panning, M. & Romanowicz, B., 2004. Inferences on flow at the base of Earth's mantle based on seismic anisotropy, *Science,* **303,** 351–353.

Panning, M. & Romanowicz, B., 2006. A three-dimensional radially anisotropic model of shear velocity in the whole mantle, *Geophys. J. Int.,* **167**(1), 361–379.

Panning, M., Lekić, V. & Romanowicz, B., 2010. Importance of crustal corrections in the development of a new global model of radial anisotropy, *J. geophys. Res.,* **115**(B12), B12325, doi:10.1029/2010JB007520.

Peter, D. & Boschi, L., 2009. Tomographic resolution of ray and finite-frequency methods: a membrane-wave investigation, *Geophys. J. Int.,* **177,** 624–638.

Peter, D., Tape, C. & Boschi, L., 2007. Surface wave tomography: global membrane waves and adjoint methods, *Geophys. J. Int.,* **171,** 1098–1117.

Pulliam, J. & Sen, M.K., 1998. Seismic anisotropy in the core–mantle transition zone, *Geophys. J. Int.,* **135,** 113–128.

Resovsky, J. & Ritzwoller, M., 1995. Constraining odd-degree Earth structure with coupled free-oscillations, *Geophys. Res. Lett.,* **22**(16), 2301–2304.

Resovsky, J. & Ritzwoller, M., 1998. New and refined constraints on three-dimensional Earth structure from normal modes below 3 mHz, *J. geophys. Res.,* **103**(B1), 783–810.

Resovsky, J. & Ritzwoller, M., 1999a. Regularization uncertainty in density models estimated from normal mode data, *Geophys. Res. Lett.,* **26**(15), 2319–2322.

Resovsky, J.S. & Ritzwoller, M.H., 1999b. A degree 8 mantle shear velocity model from normal mode observations below 3 mHz, *J. geophys. Res.,* **104**(B1), 993–1014.

Ringwood, A.E. & Irifune, T., 1988. Nature of the 650–km seismic discontinuity: implications for mantle dynamics and differentiation, *Nature,* **331,** 131–136.

Ritsema, J., van Heijst, H. & Woodhouse, J., 1999. Complex shear wave velocity structure imaged beneath Africa and Iceland, *Science,* **286,** 1925–1928.

Ritsema, J., van Heijst, H.J. & Woodhouse, J.H., 2004. Global transition zone tomography, *J. geophys. Res.,* **109,** B02302, doi:10.1029/2003JB002610.

Ritsema, J., van Heijst, H.J., Woodhouse, J.H. & Deuss, A., 2009. Long-period body wave traveltimes through the crust: implication for crustal corrections and seismic tomography, *Geophys. J. Int.,* **179**(2), 1255–1261.

Ritsema, J., Deuss, A., van Heijst, H.J. & Woodhouse, J.H., 2010. S40RTS: a degree-40 shear-velocity model for the mantle from new Rayleigh wave dispersion, teleseismic traveltime and normal-mode splitting function measurements, *Geophys. J. Int.,* **184**(3), 1223–1236.

Ritzwoller, M., Masters, G. & Gilbert, F., 1986. Observations of anomalous splitting and their interpretation in terms of aspherical structure, *J. geophys. Res.,* **91**(B10), 10 203–10 228.

Ritzwoller, M., Masters, G. & Gilbert, F., 1988. Constraining aspherical structure with low-degree interaction coefficients: application to uncoupled multiplets, *J. geophys. Res.,* **93**(B6), 6369–6396.

Robertson, G.S. & Woodhouse, J.H., 1996. Ratio of relative S to P velocity heterogeneity in the lower mantle, *J. geophys. Res.,* **101**(B9), 20 041–20 052.

Romanowicz, B., 2001. Can we resolve 3D density heterogeneity in the lower mantle, *Geophys. Res. Lett.,* **28**(6), 1107–1110.

Romanowicz, B., 2003. Global mantle tomography: progress status in the past 10 years, *Ann. Rev. Earth planet. Sci.,* **31**(1), 303–328.

Romanowicz, B., 2008. Using seismic waves to image Earth's internal structure, *Nature,* **451,** 266–268.

Romanowicz, B. & Giardini, D., 2001. The future of permanent seismic networks, *Science,* **293,** 2000–2001.

Shearer, P. & Masters, T.G., 1992. Global mapping of topography on the 660-km discontinuity, *Nature,* **355,** 791–796.

Sieminski, A., Lévêque, J.J. & Debayle, E., 2004. Can finite-frequency effects be accounted for in ray theory surface wave tomography?, *Geophys. Res. Lett.,* **31,** L24614, doi:10.1029/2004GL021402.

Sigloch, K., McQuarrie, N. & Nolet, G., 2008. Two-stage subduction history under North America inferred from multiple-frequency tomography, *Nat. Geosci.,* **1**(7), 458–462.

Simons, F.J., Nolet, G., Georgief, P., Babcock, J.M., Regier, L.A. & Davis, R.E., 2009. On the potential of recording earthquakes for global seismic tomography by low-cost autonomous instruments in the oceans, *J. geophys. Res.,* **114,** B05307, doi:10.1029/2008JB006088.

Simmons, N.A., Forte, A.M., Boschi, L. & Grand, S.P., 2010. GyPSuM: a joint tomographic model of mantle density and seismic wave speeds, *J. geophys. Res.: Solid Earth,* **115,** B12310, doi:10.1029/2010JB007631.

Spetzler, J., Trampert, J. & Snieder, R., 2002. The effect of scattering in surface wave tomography, *Geophys. J. Int.,* **149**(3), 755–767.

Su, W. & Dziewoński, A.M., 1991. Predominance of long-wavelength heterogeneity in the mantle, *Nature,* **352,** 121–126.

Su, W. & Dziewoński, A.M., 1997. Simultaneous inversion for 3-D variations in shear and bulk velocity in the mantle, *Phys. Earth planet. Inter.,* **100**(1–4), 135–156.

Su, W.-j. & Dziewoński, A.M., 1992. On the scale of mantle heterogeneity, *Phys. Earth planet. Inter.,* **74**(1–2), 29–54.

Tackley, P.J., Stevenson, D.J., Glatzmaier, G.A. & Schubert, G., 1993. Effects of an endothermic phase transition at 670 km depth in a spherical model of convection in the Earth's mantle, *Nature,* **361,** 699–704.

Takeuchi, H. & Saito, M., 1998. Seismic surface waves, in *Seismology: Surface Waves and Earth Oscillations, Methods in Comput. Phys.,* Vol. 11, pp. 217–295, ed. Bolt, B.A., Academic Press.

Tape, C., Liu, Q., Liu, Q., Maggi, A. & Tromp, J., 2009. Adjoint tomography of the Southern California Crust, *Science,* **325,** 988–992.

Tarantola, A., 1984. Linearized inversion of seismic reflection data, *Geophys. Prospect.,* **32,** 998–1015.

Tian, Y., Zhou, Y., Sigloch, K., Nolet, G. & Laske, G., 2011. Structure of North American mantle constrained by simultaneous inversion of multiple-frequency SH, SS, and Love waves, *J. geophys. Res.,* **116**(B2), B02307, doi:10.1029/2010JB007704.

Trampert, J. & Spetzler, J., 2006. Surface wave tomography: finite-frequency effects lost in the null space, *Geophys. J. Int.,* **164**(2), 394–400.

Trampert, J. & van Heijst, H.J., 2002. Global azimuthal anisotropy in the transition zone, *Science,* **296,** 1297–1299.

Trampert, J. & Woodhouse, J.H., 1995. Global phase-velocity maps of Love and Rayleigh-waves between 40 and 150 seconds, *Geophys. J. Int.,* **122,** 675–690.

Trefethen, L. & Bau, D., 1997. *Numerical Linear Algebra,* Soc. Ind. Appl. Math.

Tromp, J., 1993. Support for anisotropy of the Earths inner-core from free oscillations, *Nature,* **366,** 678–681.

Tromp, J., 1995. Normal-mode splitting due to inner-core anisotropy, *Geophys. J Int.,* **121**(3), 963–968.

Tromp, J. & Zanzerkia, E., 1995. Toroidal splitting observations from the great 1994 Bolivia and Kuril Islands earthquakes, *Geophys. Res. Lett.,* **22**(16), 2297–2300.

Tromp, J., Tape, C. & Liu, Q., 2005. Seismic tomography, adjoint methods, time reversal and banana-doughnut kernels, *Geophys. J. Int.,* **160,** 195–216.

van der Hilst, R.D. & de Hoop, M.V., 2005. Banana-doughnut kernels and mantle tomography, *Geophys. J. Int.,* **163**(3), 956–961.

van Heijst, H.J. & Woodhouse, J., 1997. Measuring surface-wave overtone phase velocities using a mode-branch stripping technique, *Geophys. J. Int.,* **131**(2), 209–230.

van der Hilst, R.D., Widiyantoro, S. & Engdahl, E.R., 1997. Evidence for deep mantle circulation from global tomography, *Nature,* **386,** 578–584.

Vinnik, L., Romanowicz, B., Le Stunff, Y. & Makeyeva, L., 1995. Seismic anisotropy in the D″ layer, *Geophys. Res. Lett.,* **22**(13), 1657–1660.

Vinnik, L., Breger, L. & Romanowicz, B., 1998. Anisotropic structures at the base of the Earth's mantle, *Nature,* **393,** 564–567.

Visser, K. & Trampert, J., 2008. Global anisotropic phase velocity maps for higher mode Love and Rayleigh waves, *Geophys. J. Int.,* **172,** 1016–1032.

Wang, Z. & Dahlen, F., 1995. Spherical-spline parameterization of 3-dimensional Earth models, *Geophys. Res. Lett.,* **22**(22), 3099–3102.

Webb, S.C., 1998. Broadband seismology and noise under the ocean, *Rev. Geophys.,* **36**(1), 105–142.

Wentzcovitch, R., Karki, B., Cococcioni, M. & de Gironcoli, S., 2004. Thermoelastic properties of $MgSiO_3$-perovskite: insights on the nature of the Earth's lower mantle, *Phys. Rev. Lett.,* **92**(1), doi:10.1103/physrevlett.92.018501.

Woodhouse, J. & Dahlen, F., 1978. The effect of a general aspherical perturbation on the free oscillations of the Earth, *Geophys. J. Int.,* **53,** 335–354.

Woodhouse, J., Giardini, D. & LI, X., 1986. Evidence for inner core anisotropy from free oscillations, *Geophys. Res. Lett.,* **13**(13), 1549–1552.

Woodhouse, J.H., 1981. A note on the calculation of travel times in a transversely isotropic earth model, *Phys. Earth planet. Inter.,* **25**(4), 357–359.

Woodhouse, J.H. & Dziewoński, A.M., 1984. Mapping the upper mantle: three-dimensional modeling of Earth structure by inversion of seismic waveforms, *J. geophys. Res.,* **89**(B7), 5953–5986.
Woodward, R.L. & Masters, G., 1991. Global upper mantle structure from long-period differential travel times, *J. geophys. Res.,* **96**(B4), 6351–6377.
Wookey, J., Kendall, J.M. & Barruol, G., 2002. Mid-mantle deformation inferred from seismic anisotropy, *Nature,* **415,** 777–780.
Wysession, M., 1996. How well do we utilize global seismicity?, *Bull. seism. Soc. Am.,* **86**(5), 1207–1219.
Yamazaki, D. & Karato, S., 2002. Fabric development in (Mg, Fe) O during large strain, shear deformation: implications for seismic anisotropy in Earth's lower mantle, *Phys. Earth planet. Inter.,* **131,** 251–267.
Yoshizawa, K. & Kennett, B., 2002a. Non-linear waveform inversion for surface waves with a neighbourhood algorithm—application to multimode dispersion measurements, *Geophys. J. Int.,* **149,** 118–133.
Yoshizawa, K. & Kennett, B.L.N., 2002b. Determination of the influence zone for surface wave paths, *Geophys. J. Int.,* **149**(2), 440–453.
Yuan, K. & Beghein, C., 2013. Seismic anisotropy changes across upper mantle phase transitions, *Earth planet. Sci. Lett.,* **374,** 132–144.
Zha, C.-s., Duffy, T.S., Mao, H.-k., Downs, R.T., Hemley, R.J. & Weidner, D.J., 1997. Single-crystal elasticity of $\beta$-$Mg_2SiO_4$ to the pressure of the 410 km seismic discontinuity in the Earth's mantle, *Earth planet. Sci. Lett.,* **147,** E9–E15.
Zhang, Y.S. & Lay, T., 1996. Global surface wave phase velocity variations, *J. geophys. Res.,* **101**(B4), 8415–8436.
Zhao, L., Jordan, T. & Chapman, C.H., 2000. Three-dimensional Fréchet differential kernels for seismicdelay times, *Geophys. J. Int.,* **141,** 558–576.
Zhu, H., Bozdağ, E., Peter, D. & Tromp, J., 2012. Structure of the European upper mantle revealed by adjoint tomography, *Nat. Geosci.*, **5**(7), 493–498.

## APPENDIX: PROJECTION MATRIX BETWEEN SPHERICAL SPLINES AND HARMONICS

The lateral variations in the Earth's structure or global data sets such as surface wave phase velocity maps and normal-mode splitting functions can be expressed either in terms of spherical harmonics or localized splines. The selection between the two depends on the imaging requirements and the coverage of the data. Here, we give the expressions of the two types of basis functions and the projection matrix to convert between them. In this study, the model parameters, $c_{ij}$ from eq. (11), are in terms of spherical splines, while the mode-splitting data are in terms of spherical harmonic coefficients $c_{st}$ from eqs (1) and (2). The splitting functions $F(\theta, \phi)$ can be denoted as a complex square-integrable function on the surface of a unit sphere $\psi(\theta, \phi)$ with Laplace coefficients $\psi_{lm}$. Such functions can be expressed as

$$\psi(\theta,\phi) = \sum_{l=0}^{\infty}\sum_{m=-l}^{l} \psi_{lm} Y_{lm}(\theta,\phi) \text{ where } \psi_{lm} = \int_{\Omega} Y^*_{lm}\psi \,\mathrm{d}\Omega, \tag{A1}$$

where $Y^*_{lm}$ are the complex conjugate of the spherical harmonic functions $Y_{lm}$.

Using the spherical harmonic expansions from Dahlen & Tromp (1998) and eqs (11) and (A1), we can write the equivalent model coefficients, $c_{lm}$, as

$$c_{lm} = \int_{\Omega} Y^*_{lm}\frac{\delta m_0}{m_0}\mathrm{d}\Omega = \sum_j c_{ij}\int_{\Omega} Y^*_{lm}S_j(\theta,\phi)\mathrm{d}\Omega = \sum_j c_{ij}P^{st}_j \tag{A2}$$

where $P^{st}_j$ is the projection matrix that relates the model coefficients in spherical splines, $c_{ij}$, to the equivalent ones in spherical harmonics $c_{lm}$. The predictions of the splitting coefficients from spline parametrized models such as S362ANI are made using this relation and eq. (1). We perform the integration on the $P^{st}_j$ term by specifying on the unit sphere, a grid containing 180 longitudinal and 90 latitudinal zones.

Since we use real spherical harmonics (e.g Dahlen & Tromp 1998, Appendix B), $Y^*_{lm}$ in eqs (A1) and (A2) equal $Y_{lm}$, which are defined at a location $(\theta, \phi)$ as

$$Y_{lm}(\theta,\phi) = \begin{cases} \sqrt{2}X_{l|m|}(\theta)\cos m\phi & \text{if } -l \le m < 0, \\ X_{l0}(\theta) & \text{if } m = 0, \\ \sqrt{2}X_{lm}(\theta)\sin m\phi & \text{if } 0 < m \le l, \end{cases} \tag{A3}$$

where $X_{st}(\theta, \phi)$ is the associated normalized Legendre function of degree $l$ and order $m$. In these equations, the degree $l$ is equivalent to $s$ and order $m$ to $t$ in eqs (1)–(7).